EPFL

ÉCOLE POLYTECHNIQUE FÉDÉRALE DE LAUSANNE

On improving the evaluation of the gyrokinetic moment expanded collision operator

EPFL SWISS PLASMA CENTER

Antonino Emanuele Scurria

November 1, 2024

Abstract

Studying the nonlinear effects of plasma dynamics with arbitrary collisionality is a key focus in fusion research. This is especially crucial in the periphery of magnetic confinement fusion devices, where instabilities of varying scales, from the Larmor radius to the device's size, are expected. Coulombian collisions dominate particle-particle interactions in this region. Replicating such phenomena poses a challenge for numerical simulations, prompting the exploration of various solutions.

This research project centers on investigating approximations of a pseudo-spectral numerical scheme, the gyromoment approach. Specifically, after an introduction to the gyromoment method, we will focus on finding specific filters for the matricial representation of the linear Coulomb collision operator in the drift kinetic limit to lower the computational complexity of the simulation. After the development of the filters, we will test the performance of the new approximation in the drift kinetic limit with different metrics, obtaining a good overall performance. In the end, we can affirm that we are able to lower the computational complexity from $O(N^2)$ to $O(N)$ in the number of moments for the electrons-electrons moments matrix.

1 Introduction

In this first section we will describe the gyromoment expansion of the collision operator following the derivation presented in [1]. As a starting point, we consider the electrostatic gyrokinetic (GK) Boltzmann equation in the presence of a magnetic field, density, and temperature gradients. We use gyrocenter phase-space coordinates denoted as $\boldsymbol{Z} = \left(\boldsymbol{R}, \mu, v_\parallel, \theta\right)$, where $\boldsymbol{R} = \boldsymbol{r} - \boldsymbol{\rho}_a$ represents the gyrocenter position (with a as the species index), where $\boldsymbol{r}$ is the particle position, and $\rho_a(\boldsymbol{R}, \mu, \theta) = \boldsymbol{b} \times \boldsymbol{v}/\Omega_a$ signifies the gyroradius of species a (with $\boldsymbol{b} = \boldsymbol{B}/B$ and $\Omega_a = q_a B/m_a$), $\mu = m_a v_\perp^2/[2B(\boldsymbol{R})]$ is the magnetic moment, $v_\parallel = \boldsymbol{b} \cdot \boldsymbol{v}$ represents the component of velocity parallel to the magnetic field, and θ denotes the gyroangle.

Then we consider the linearized the GK Boltzmann equation by assuming the gyrocenter distribution function of species a, $F_a = F_a\left(\boldsymbol{R}, \mu, v_\parallel\right)$, is a perturbed Maxwellian, given by $F_a = F_{Ma} + g_a$, where $g_a = g_a\left(\boldsymbol{R}, \mu, v_\parallel, t\right)$ represents the perturbation with respect to the local Maxwellian distribution function $F_{Ma} = N \exp\left(-s_{\parallel a}^2 - x_a\right)/\left(\pi^{3/2} v_{Ta}^3\right)$. Here, $g_a/F_{Ma} \ll 1$, with $N = N_i(\boldsymbol{R}) = N_e(\boldsymbol{R})$ representing the background gyrocenter density, $s_{\parallel a} = v_\parallel/v_{Ta}(\boldsymbol{R})$, $x_a = \mu B(\boldsymbol{R})/T_a(\boldsymbol{R})$, and $v_{T_0}^2(\boldsymbol{R}) = 2T_a(\boldsymbol{R})/m_a$ representing the thermal velocity based on the equilibrium temperature $T_a(\boldsymbol{R})$.

The linearized electrostatic GK Boltzmann equation describing the time evolution of $g_a(\boldsymbol{k}, t) = \int \mathrm{d}\boldsymbol{R} g_a(\boldsymbol{R}, t) \exp(-\mathrm{i}\boldsymbol{R} \cdot \boldsymbol{k})$ can be expressed as [2].

$$\frac{\partial}{\partial t} g_a + \mathrm{i}\omega_{Ba} h_a + v_\parallel \nabla_\parallel h_a - \frac{\mu}{m_s}(\boldsymbol{b} \cdot \nabla B)\frac{\partial}{\partial v_\parallel} h_a - \mathrm{i}\omega_{Ta}^* \, \mathrm{J}_0\left(b_a\sqrt{x_a}\right)\phi F_{Ma} = \sum_b \mathcal{C}_{ab} \quad (1)$$

where $\phi = \phi(\boldsymbol{k}, t)$ is the Fourier component of the electrostatic potential and we use the non-adiabatic part, $h_a = h_a\left(\boldsymbol{k}, \mu, v_\parallel, t\right)$, as presented in [1], of the perturbed gyrocentre distribution function g_a, that is

$$h_a = g_a + \frac{q_a}{T_a} F_{Ma} \, \mathrm{J}_0\left(b_a\sqrt{x_a}\right)\phi \quad (2)$$

In 1, we set $\nabla_\parallel = \boldsymbol{b} \cdot \nabla, \omega_{Ba} = v_{Ta}^2\left(x_a + 2s_{\parallel a}^2\right)\omega_B/\left(2\Omega_a\right)$, with $\omega_B = (\boldsymbol{b} \times \nabla \ln B) \cdot \boldsymbol{k}$, and $\omega_{Ta}^* = \left[\omega_N + \omega_{Ta}\left(x_a + s_{\parallel a}^2 - 3/2\right)\right]$, with $\omega_N = \boldsymbol{b} \times \nabla \ln N \cdot \boldsymbol{k}/B$ and $\omega_{Ta} = \boldsymbol{b} \times \nabla \ln T_a \cdot \boldsymbol{k}/B$. Finite Larmor radius effects are taken into account through the zeroth-order Bessel function, $\mathrm{J}_0\left(b_a\sqrt{x_a}\right)$, where $b_a = k_\perp v_{Ta}/\Omega_a$ is the normalized perpendicular wavevector, with $k_\perp = |\boldsymbol{k} - (\boldsymbol{b} \cdot \boldsymbol{k})\boldsymbol{b}|$. On the right-hand side of 1, we define the linearized GK collision operator between species a and b, $\mathcal{C}_{ab} = \mathcal{C}_{ab}\left(\boldsymbol{R}, \mu, v_\parallel\right)$,

$$\mathcal{C}_{ab} = \langle C_{ab}\rangle_R = \frac{1}{2\pi}\int_0^{2\pi} \mathrm{d}\theta C_{ab} \quad (3)$$

One can observe that the linearized GK collision operator is thus gyrophase independent and it is a function only of the gyrocentre phase space, i.e. $\mathcal{C}_{ab} = \mathcal{C}_{ab}\left(\boldsymbol{R}, \mu, v_\parallel\right)$: this means that we do not take into account the precise position of the particle around its gyrocentre but we compute an average value on the gyrophase.

Then we close the linearized Boltzmann equation by the GK quasineutrality condition that determines self-consistently the electrostatic potential,

$$\sum_a \frac{q_a^2}{T_a} \left[1 - \Gamma_0\left(a_a\right)\right]\phi = \sum_a q_a \int \mathrm{d}\mu \mathrm{d}v_\parallel \mathrm{d}\theta \frac{B}{m_a} \, \mathrm{J}_0\left(b_a\sqrt{x_a}\right)g_a \tag{4}$$

where $a_a = b_a^2/2$, and $\Gamma_0(x) = \mathrm{I}_0(x)\mathrm{e}^{-x}$ with I_0 the modified Bessel function.

Now that we have defined the problem to solve, our strategy, the gyromoment approach, consists in projecting both sides of the equation 1and 4 onto a specific basis using the Hermite-Laguerre moment expansion of the gyrocentre , we use a Hermite-Laguerre moment expansion of the gyrocentre perturbed distribution function g_a ([3] and [4]). Then, by projecting 1 onto the Hermite-Laguerre basis polynomials, we reduce its dimensionality removing the $\left(\mu, v_\parallel\right)$dependence.

$$g_a = \sum_{p=0}^{\infty} \sum_{j=0}^{\infty} N_a^{pj} \frac{H_p\left(s_{\parallel a}\right) L_j\left(x_a\right)}{\sqrt{2^p p!}} F_{Ma} \tag{5}$$

where the Hermite-Laguerre velocity moments of g_a are defined as

$$N_a^{pj} = \frac{1}{N_a} \int \mathrm{d}\mu \mathrm{d}v_\parallel \mathrm{d}\theta \frac{B}{m_a} g_a \frac{H_p\left(s_{\parallel a}\right) L_j\left(x_a\right)}{\sqrt{2^p p!}} \tag{6}$$

with $N_a = \int \mathrm{d}\mu \mathrm{d}v_\parallel \mathrm{d}\theta B g_a/m_a$ the gyrocentre density. In 6, we use the Rodrigues'formula to represent the Hermite and Laguerre polynomials, H_p and L_j

$$H_p(x) = (-1)^p \mathrm{e}^{x^2} \frac{\mathrm{d}^p}{\mathrm{d}x^p}\left(\mathrm{e}^{-x^2}\right),$$

$$L_j(x) = \frac{\mathrm{e}^x}{j!} \frac{\mathrm{d}^j}{\mathrm{d}x^j}\left(\mathrm{e}^{-x}x^j\right)$$

and we recall their weighted orthogonality relations, respectively,

$$\int_{-\infty}^{\infty} \mathrm{d}x H_p(x) H_{p'}(x)\mathrm{e}^{-x^2} = 2^p p!\sqrt{\pi}\delta_p^{p'},$$

$$\int_0^{\infty} \mathrm{d}x L_j(x) L_{j'}(x)\mathrm{e}^{-x} = \delta_j^{j'}.$$

The Hermite-Laguerre coefficients, N_a^{pj} in 6, are called the gyromoments. Moreover we are sure that such an expansion exists since any function, $f = f\left(\mu, v_\parallel\right)$, that satisfies

$$\int \mathrm{d}\mu \mathrm{d}v_\parallel \mathrm{d}\theta \frac{B}{m_a}|f|^2 \mathrm{e}^{-s_{\parallel a}^2 - x_a} < +\infty,$$

can be decomposed onto the orthogonal basis defined by the Hermite-Laguerre polynomials [5] and this is fulfilled by the perturbed gyrocentre distribution function g_a and by its non-adiabatic part, h_a.

We now have to project both equations 1 and 4 onto the Hermite-Laguerre basis. For this we exploit the fact that there exists an expansion of the Bessel functions J_m , $m >= 0$ through associated Laguerre polynomials, $L_n^m(x) = (-1)^m d^m L_{n+m}(x)/\mathrm{d}x^m$ [6].

$$\mathrm{J}_m\left(b_a\sqrt{x_a}\right) = \left(\frac{b_a\sqrt{x_a}}{2}\right)^m \sum_{n=0}^{\infty} \frac{n!\mathcal{K}_n\left(b_a\right)}{(n+m)!} L_n^m\left(x_a\right)$$

where we define the velocity-independent expansion coefficients as

$$\mathcal{K}_n\left(b_a\right) = \frac{1}{n!}\left(\frac{b_a}{2}\right)^{2n} \mathrm{e}^{-b_a^2/4}$$

Now, multiplying the GK Boltzmann equation 1 by the basis element $BH_p\left(s_{\|a}\right)L_j\left(x_a\right)/\sqrt{2^p p}$!, and integrating over the velocity space yields the gyromoment hierarchy equation,

$$
\begin{aligned}
&\frac{\partial}{\partial t}N_a^{pj} + v_{Ta}\nabla_\|\left(\sqrt{\frac{p+1}{2}}n_a^{p+1j} + \sqrt{\frac{p}{2}}n_a^{p-1j}\right)\\
&- v_{Ta}\nabla_\| \ln B\left[(j+1)\sqrt{p+1}n_a^{p+1j} + (j+1)\sqrt{p}n_a^{p-1j} - j\sqrt{p+1}n_a^{p+1j-1} - j\sqrt{p}n_a^{p-1j-1}\right]\\
&+ \frac{T_a\mathrm{i}\omega_B}{q_a B}\left[\sqrt{(p+1)(p+2)}n_a^{p+2j} + (2p+1)n_a^{pj} + \sqrt{p(p-1)}n_a^{p-2j}\right.\\
&+ (2j+1)n_a^{pj} - jn_a^{pj-1} - (j+1)n_a^{pj+1}\Big]\\
&+ v_{Ta}\nabla_\| \ln B\sqrt{\frac{p}{2}}\left[(2j+1)n_a^{p-1j} - (j+1)n_a^{p-1j+1} - jn_a^{p-1j-1}\right]\\
&- \mathrm{i}\phi\left\{\mathcal{K}_j\delta_p^0\omega_N + \omega_{Ta}\left[\mathcal{K}_j\left(\frac{\delta_p^2}{\sqrt{2}} - \delta_p^0\right) + \delta_p^0\left((2j+1)\mathcal{K}_j - j\mathcal{K}_{j-1} - (j+1)\mathcal{K}_{j+1}\right)\right]\right\}\\
&= \sum_b \mathcal{C}_{ab}^{pj}
\end{aligned}
$$

(7)

where $\mathcal{C}_{ab}^{pj} = \mathcal{C}_{ab}^{pj}(\boldsymbol{R}, t)$ is the expansion of the linearized GK collision operator $\mathcal{C}_{ab}$ through the Hermite-Laguerre basis.

$$\mathcal{C}_{ab}^{pj} = \int \mathrm{d}\theta \mathrm{d}\mu \mathrm{d}v_\| \frac{B}{m_a}\frac{H_p\left(s_{\|a}\right)L_j\left(x_a\right)}{\sqrt{2^p p!}}\mathcal{C}_{ab} \tag{8}$$

In 7, the non-adiabatic gyromoments n_a^{pj}, are defined by

$$n_a^{pj} = \frac{1}{N_a}\int \mathrm{d}\mu \mathrm{d}v_\| \mathrm{d}\theta \frac{B}{m_a}h_a \frac{H_p\left(s_{\|a}\right)L_j\left(x_a\right)}{\sqrt{2^p p!}} \tag{9}$$

We can further express the non-adiabatic gyromoments in terms of the gyromoments N_a^{pj} by projecting 2 onto the Hermite-Laguerre basis, yielding

$$n_a^{pj} = N_a^{pj} + \frac{q_a}{T_a}\mathcal{K}_j\phi\delta_p^0$$

Finally, 4 projected onto the Hermite-Laguerre basis has the form

$$\sum_a \frac{q_a^2}{T_a}\left(1 - \sum_{n=0}^\infty \mathcal{K}_n^2\left(b_a\right)\right)\phi = \sum_a q_a N_a \sum_{n=0}^\infty \mathcal{K}_n\left(b_a\right)N_a^{0n} \tag{10}$$

4

1.1 Linearized Gyrokinetic Coulomb collision operator

In a broader context, the derivation of the linearized collision operator between particles of species a and b, denoted as C_{ab}, involves linearizing a nonlinear collision operator, C_{ab}^{NL}. Nonlinear collision operators are conventionally defined in terms of the complete particle distribution function expressed in the particle phase space $(\boldsymbol{r}, \boldsymbol{v})$. This choice is made because collisions primarily occur at the particle position $\boldsymbol{r}$ rather than the gyrocenter position $\boldsymbol{R}$. Given $f_{Ma} = f_{Ma}(\boldsymbol{r}, \boldsymbol{v})$, the particle Maxwellian distribution function of species a, and $f_a = f_a(\boldsymbol{r}, \boldsymbol{v})$ representing its small amplitude perturbation with $f_a/f_{Ma} \ll 1$, the linearized collision operator, $C_{ab} = C_{ab}(\boldsymbol{r}, \boldsymbol{v}) = C_{ab}(f_a, f_b)$, can be decomposed as

$$C_{ab} = C_{ab}^T + C_{ab}^F$$

Here, we introduce the test component of the linearized collision operator, $C_{ab}^T = C_{ab}^T(\boldsymbol{r}, \boldsymbol{v}) = C_{ab}^T(f_a(\boldsymbol{r}, \boldsymbol{v})) = C^{NL}(f_a, f_{Mb})$, and the field component, $C_{ab}^F = C_{ab}^F(\boldsymbol{r}, \boldsymbol{v}) = C_{ab}^F(f_b(\boldsymbol{r}, \boldsymbol{v})) = C^{NL}(f_{Ma}, f_b)$. Thus we understand why we use the 'linear' term: in introducing the test and field component we are simply neglecting the contribution of the non linear collision operator that arise from the 'interaction' of both the probability density perturbations since we are assuming them small. Moreover the conservation properties of the collision operator imply the following relations for the test and field component [7], leading to

$$\int \mathrm{d}v\, C_{ab}^T = \int \mathrm{d}v\, C_{ab}^F = 0$$

Moreover, momentum and energy conservation necessitate that

$$\int \mathrm{d}\boldsymbol{v}\, m_a v\, C_{ab}^T + \int \mathrm{d}\boldsymbol{v}\, m_b v\, C_{ba}^F = 0$$

$$\int \mathrm{d}v\, m_a v^2\, C_{ab}^T + \int \mathrm{d}v\, m_b v^2\, C_{ba}^F = 0$$

respectively. We underline that his conservation laws are evaluated at constant $\boldsymbol{r}$, and that local conservation laws do not hold in the gyrocentre coordinates $\left(\boldsymbol{R}, \mu, v_\parallel, \theta\right)$, because of $\boldsymbol{r} - \boldsymbol{R} = \boldsymbol{\rho}_a(\boldsymbol{R}, \mu, \theta) \neq 0$. However, in the DK limit, because of negligible finite $\boldsymbol{k} \cdot \boldsymbol{\rho}_a$ effects, we have $\langle C_{ab}(\boldsymbol{r}, \boldsymbol{v})\rangle_{\boldsymbol{R}} \simeq \langle C_{ab}(\boldsymbol{R}, \boldsymbol{v})\rangle_{\boldsymbol{R}}$, and the previous conservation laws for the gyrocentre positions are satisfied.

Now that we have briefly presented some central concepts for collision operators, we will focus on the Hermite-Laguerre expansion for the linearized GK Coulomb collision operator [8]. Initially, we will follow the ideas presented in [8] presenting tha main steps: the first step will be and expansion of the collision operator through spherical harmonics; then we will perform a change of basis to project the spherical harmonics expansion onto the Hermite-Laguerre polynomial basis.

Finally, we obtain the DK limit by explicitly considering the zeroth gyroradius limit, i.e., $\boldsymbol{k} \cdot \boldsymbol{\rho}_a \to 0$.

As previously stated, we start from the nonlinear Coulomb collision operator: for this operator the test component of the linearized Coulomb collision operator around a local particle Maxwellian distribution function, f_{Mb}, is given in the particle pitch-angle coordinates $(\boldsymbol{r}, v, \xi, \theta)$ (with v the modulus of v and $\xi = v_\parallel/v$ the pitch angle) by ([9]; [10]; [2])

$$C_{ab}^T (f_a) = \frac{m_a v_{ab} v_{Ta}}{n_b} \left[\left(\frac{2\partial_v G (f_{Mb})}{v^2} + \left(1 - \frac{m_a}{m_b}\right) \partial_v H (f_{Mb}) \right) \partial_v f_a \right.$$

$$\left. - \frac{1}{v^3} \partial_v G (f_{Mb}) \mathcal{L}^2 f_a + \partial_v^2 G (f_{Mb}) \partial_v^2 f_a + \frac{m_a}{m_b} 8\pi f_{Mb} f_a \right]. \tag{11}$$

The field component, expressed in the particle coordinates, $(\boldsymbol{r}, v, \xi, \theta)$, has the form

$$C_{ab}^F (f_b) = \frac{2 v_{ab} v_{Ta} f_{Ma}}{n_b} \left[2 s_a^2 \partial_v^2 G (f_b) - H (f_b) - \left(1 - \frac{m_a}{m_b}\right) v \partial_v H (f_b) + \frac{m_a}{m_b} 4\pi v_{Ta}^2 f_b \right]. \tag{12}$$

In the formulas of the test and field components, we use the definition of the Rosenbluth potentials $H(f) = 2 \int d\boldsymbol{v}' f (\boldsymbol{v}') / u$ and $G(f) = \int d\boldsymbol{v}' f (\boldsymbol{v}') u$ (with $u = |\boldsymbol{v} - \boldsymbol{v}'|$), the collision frequency between species a and b, $v_{ab} = 4\sqrt{\pi} N_b q_a^2 q_b^2 \ln \Lambda / \left(3 m_a^{1/2} T_a^{3/2}\right)$ and the spherical angular operator $\mathcal{L}^2 f = \partial_v \left(v^2 \partial_v f\right) - v^2 \nabla_v^2 f$. Finally, the thermal velocity is defined as $v_{Ta}^2 = 2 T_a / m_a$. A particular case of interest for the evaluation of the Rosenbluth potentials is the case of Maxwellian distribution where the potentials are given by $H (f_{Mb}) = 2 n_b \operatorname{erf} (s_b) / v$ and $G (f_{Mb}) = n_b v_{Tb} \left[\left(1 + 2 s_b^2\right) \operatorname{erf} (s_b) / s_b + \operatorname{erf}' (s_b)\right] / 2$, with $s_b = v / v_{Tb}$, the error function,

Equations 11 and 12 are respectively referred to as the exact test and field components of the Coulomb collision operator between species a and b [9].

1.1.1 Spherical harmonics moment expansion

As previously stated we will first present the spherical harmonics expansion following [11] [8]. To do so, we start by expanding the perturbed particle distribution function of species a, $f_a = f_a(\boldsymbol{x}, \boldsymbol{v})$, in the spherical harmonics basis as

$$f_a = \sum_{p=0}^{\infty} \sum_{j=0}^{\infty} \frac{f_{Ma}}{\sigma_j^p} \boldsymbol{M}_a^{pj} \cdot \boldsymbol{Y}^p (\boldsymbol{s}_a) L_j^{p+1/2} (s_a^2) \tag{13}$$

with $\sigma_j^p = p!(p+j+1/2)! / \left[2^p (p + 1/2)! j!\right]$ and $s_a = v / v_{Ta}$. We remark that the quantities $\boldsymbol{M}_a^{pj}$ are defined below in (3.14). In equation 13, the velocity-space basis, $\boldsymbol{Y}^p (\boldsymbol{s}_a) L_j^{p+1/2} (s_a^2)$, is the product between the p th-order traceless symmetric spherical harmonic tensors, $\boldsymbol{Y}^p (\boldsymbol{s}_a)$, and the associated Laguerre polynomials, $L_j^{p+1/2} (s_s^2)$, that are defined as [6]

$$L_j^{p+1/2}(x) = \sum_{l=0}^{j} L_{jl}^p x^l \tag{14}$$

with

$$L_{jl}^p = \frac{(-1)^l (p + j + 1/2)!}{(j - l)!(l + p + 1/2)! l!} \tag{15}$$

. The spherical harmonic tensors have the property that $\nabla_v^2 \boldsymbol{Y}^p = 0$, such that $\mathcal{L}^2 \boldsymbol{Y}^p = p(p + 1)\boldsymbol{Y}^p$ and $\boldsymbol{Y}^p(\boldsymbol{v}) = v^p \boldsymbol{Y}^p(\hat{\boldsymbol{v}})(\hat{\boldsymbol{v}} = \boldsymbol{v}/v)$ [8], and can be defined by introducing the spherical harmonic basis, $\boldsymbol{e}^{pm}$, that satisfies the orthogonality relation $\boldsymbol{e}^{pm} \cdot \boldsymbol{e}^{pm'} = (-1)^m \delta_{-m}^{m'}$ [12]. The expression of the spherical harmonic tensors, $\boldsymbol{Y}^p (\boldsymbol{s}_a)$, on that basis is

$$\boldsymbol{Y}^p\left(\boldsymbol{s}_a\right) = s_a^p \sqrt{\frac{2\pi^{3/2}p!}{2^p(p+1/2)!}} \sum_{m=-p}^{p} Y_p^m(\xi,\theta)\boldsymbol{e}^{pm} \tag{16}$$

where

$$Y_p^m(\xi,\theta) = \sqrt{\frac{(2p+1)(p-|m|)!}{4\pi(p+|m|)!}} P_p^m(\xi)\mathrm{e}^{\mathrm{i}m\theta} \tag{17}$$

are scalar harmonic functions, with $P_p^m(\xi) = (-1)^m \left(1-\xi^2\right)^{m/2} \mathrm{d}^m P_p(\xi)/\mathrm{d}\xi^m$ the associated Legendre polynomials, and $P_p(\xi) = \mathrm{d}^p\left[\left(\xi^2-1\right)^p\right]/\mathrm{d}\xi^p/\left[2^p p!\right]$ the Legendre polynomial [6]. We observe that the expansion 13 is useful since it allows use to isolate the θ dependence in $Y_p^m(\xi,\theta)$ and to compute analytically the gyroaverage. Then using an orthogonality relation presented in [12], projecting the spherical harmonic basis and using 13, one obtains the expansion coefficient $\boldsymbol{M}_a^{pj} = \boldsymbol{M}_a^{pj}(\boldsymbol{r})$, defined as the spherical harmonic particle moments of species a:

$$\boldsymbol{M}_a^{pj} = \frac{1}{n_a} \int \mathrm{d}\boldsymbol{v}\, f_a \boldsymbol{Y}^p\left(\boldsymbol{s}_a\right) L_j^{p+1/2}\left(s_a^2\right) \tag{18}$$

with n_a the particle density background of species a, with $n_a = N_a$.

Now we can insert this expansion in the Rosenbluth potentials, $H\left(f_b\right)$ and $G\left(f_b\right)$ to obtain [8],

$$H\left(f_b\right) = \frac{4n_b}{v_{Tb}} \sum_{p=0}^{\infty} \sum_{j=0}^{\infty} \sum_{m=0}^{j} \frac{L_{jm}^p}{\sigma_p^j} \frac{\boldsymbol{Y}^p\left(\hat{\boldsymbol{s}}_b\right)\cdot\boldsymbol{M}_b^{pj}}{2p+1} \left[\frac{\mathrm{I}_-^{2p+2m+2}}{s_b^{p+1}} + s_b^p \mathrm{I}_+^{2m+1}\right],$$

$$G\left(f_b\right) = 2n_b v_{Tb} \sum_{p=0}^{\infty} \sum_{j=0}^{\infty} \sum_{l=0}^{j} \frac{L_{jl}^p}{\sigma_j^p} \frac{\boldsymbol{M}_b^{pj}\cdot\boldsymbol{Y}^p\left(\hat{\boldsymbol{s}_b}\right)}{(2p+1)} \tag{19}$$

$$\times \left[\frac{1}{(2p+3)}\left(\frac{\mathrm{I}_-^{2p+2l+4}}{s_b^{p+1}} + s_b^{p+2}\mathrm{I}_+^{2l+1}\right) - \frac{1}{(2p-1)}\left(\frac{\mathrm{I}_-^{2p+2l+2}}{s_b^{p-1}} + s_b^p\mathrm{I}_+^{2l+3}\right)\right],$$

with $\hat{s}_a = s_a/s_a$ and the upper and lower incomplete gamma functions defined by $\mathrm{I}_-^k = \int_0^x \mathrm{d}s\, s^{(k-1)/2}\mathrm{e}^{-s}/\sqrt{\pi}$ and $\mathrm{I}_+^k = \int_x^{\infty} \mathrm{d}s\, s^{(k-1)/2}\mathrm{e}^{-s}/\sqrt{\pi}$, respectively.

Then, using 19 we can easily compute the velocity derivatives of the two potentials (they are required in the field component 12, and are given by

$$\frac{\partial}{\partial s_b} H_b\left(f_b\right) = \frac{4n_b}{v_{Tb}} \sum_{p=0}^{\infty} \sum_{j=0}^{\infty} \sum_{m=0}^{j} \frac{L_{jm}^p}{\sigma_p^j} \frac{\boldsymbol{Y}^p\left(\hat{\boldsymbol{s}}_b\right)\cdot\boldsymbol{M}_b^{pj}}{2p+1} \left[-(p+1)\frac{\mathrm{I}_-^{2p+2m+2}}{s_b^{p+2}} + ps_b^{p-1}\mathrm{I}_+^{2m+1}\right],$$

$$\frac{\partial^2}{\partial s_b^2} G_b\left(f_b\right) = 2n_b v_{Tb} \sum_{p=0}^{\infty} \sum_{j=0}^{\infty} \sum_{l=0}^{j} \frac{L_{jl}^p}{\sigma_j^p} \frac{\boldsymbol{M}_b^{pj}\cdot\boldsymbol{Y}^p\left(\hat{\boldsymbol{s}}_b\right)}{(2p+1)} \left[\frac{(p+1)(p+2)}{(2p+3)}\left(\frac{\mathrm{I}_-^{2p+2l+4}}{s_b^{p+3}} + s_b^p\mathrm{I}_+^{2l+1}\right)\right.$$

$$\left. -\frac{p(p-1)}{(2p-1)}\left(\frac{\mathrm{I}_-^{2p+2l+2}}{s_b^{p+1}} + s_b^{p-2}\mathrm{I}_+^{2l+3}\right)\right],$$

7

respectively. Finally, inserting the spherical harmonics expansion of f_a in 11 and 12, we obtain the spherical harmonic moment expansion of the test and field components of the linearized Coulomb collision operator C_{ab},

$$
\begin{aligned}
C_{ab}^T &= \sum_{p=0}^{\infty} \sum_{j=0}^{\infty} \frac{f_{Ma}}{\sigma_j^p} \boldsymbol{M}_a^{pj} \cdot \boldsymbol{Y}^p(\hat{\boldsymbol{v}}) \nu_{ab}^{Tpj}, \\
C_{ab}^F &= \sum_{p=0}^{\infty} \sum_{j=0}^{\infty} \frac{f_{Mb}}{\sigma_j^p} \boldsymbol{M}_b^{pj} \cdot \boldsymbol{Y}^p(\hat{\boldsymbol{v}}) \nu_{ab}^{Fpj},
\end{aligned}
\tag{20}
$$

where the test and field speed functions, v_{ab}^{Tpj} and v_{ab}^{Fpj}, are defined in the Appendix A of [1].

The next step is to compute the gyroaverage of the test component of the linearized Coulomb operator in 20. Since the gyroaverage of C_{ab} is performed at constant $\boldsymbol{R}$, we need to make the dependence on $\boldsymbol{R}$ of $\boldsymbol{M}_a^{pj}(\boldsymbol{r})$ explicit. Since $\boldsymbol{r} = \boldsymbol{R} + \boldsymbol{\rho}_a$, we can compute the gyroaverage in Fourier space by observing that $\boldsymbol{M}_a^{pj}(\boldsymbol{r}) = \int \mathrm{d}\boldsymbol{k} \boldsymbol{M}_a^{pj} \mathrm{e}^{\mathrm{i}\boldsymbol{k}\cdot\rho_a} \mathrm{e}^{\mathrm{i}\boldsymbol{k}\cdot\boldsymbol{R}}$ and by using the Jacobi-Anger identity to express the phase factor difference $\exp(\mathrm{i}\boldsymbol{k}\cdot\boldsymbol{\rho}_a) = \sum_n i^n \mathrm{J}_n(b_a\sqrt{x_a}) \mathrm{e}^{\mathrm{i}n\theta}$ [6]. Thus, in Fourier space, the linearized test component of the Coulomb collision operator at $\boldsymbol{R}$ can be written as

$$
C_{ab}^T = \sum_{p=0}^{\infty} \sum_{p=j}^{\infty} \sum_{n=-\infty}^{\infty} \frac{F_{Ma}}{\sigma_j^p} \boldsymbol{M}_a^{pj} \cdot \boldsymbol{Y}^p(\hat{\boldsymbol{v}}) i^n \mathrm{J}_n(b_a\sqrt{x_a}) \mathrm{e}^{\mathrm{i}n\theta} v_{ab}^{Tpj}
$$

and expanding $\boldsymbol{Y}^p$ first using 16:

$$
\begin{aligned}
\langle C_{ab}^T \rangle_R = \sum_{p=0}^{\infty} \sum_{j=0}^{\infty} \sum_{m=-p}^{p} \sum_{n=-\infty}^{\infty} \frac{1}{\sigma_p^j} \sqrt{\frac{2\pi^{3/2} p!}{2^p(p+1/2)!}} F_{Ma} v_{ab}^{Tpj} i^n J_n(b_a\sqrt{x_a}) \\
\times \left\langle \mathrm{e}^{\mathrm{i}n\theta} Y_p^m(\xi,\theta) \right\rangle_R \boldsymbol{M}_a^{pj} \cdot \boldsymbol{e}^{pm}.
\end{aligned}
$$

and then using the scalar harmonic functions 17 we finally obtain:

$$
\begin{aligned}
\langle C_{ab}^T \rangle_R = \sum_{p=0}^{\infty} \sum_{j=0}^{\infty} \sum_{m=-p}^{p} \frac{1}{\sigma_p^j} F_{Ma} v_{ab}^{Tpj} i^m J_m(\sqrt{x_a}b_a) \sqrt{\frac{\pi^{1/2} p!}{2^p(p-1/2)!}} \\
\times \sqrt{\frac{(p-|m|)!}{(p+|m|)!}} P_p^m(\xi) \boldsymbol{M}_a^{pj} \cdot \boldsymbol{e}^{pm}.
\end{aligned}
\tag{21}
$$

The derivation for the test component is analogous (we need to substitute $v_{ab}^{Tpj}(v)$ by $v_{ab}^{Fpj}(v)$ and $\boldsymbol{M}_a^{pj}$ by $\boldsymbol{M}_b^{pj}$). The gyroaverage for the expansion of the test component then reads:

$$
\begin{aligned}
\langle C_{ab}^F \rangle_R = \sum_{p=0}^{\infty} \sum_{j=0}^{\infty} \sum_{m=-p}^{p} \frac{1}{\sigma_p^j} F_{Ma} v_{ab}^{Fpj} i^m \mathbf{J}_m(\sqrt{x_a}b_a) \sqrt{\frac{\pi^{1/2} p!}{2^p(p-1/2)!}} \\
\times \sqrt{\frac{(p-|m|)!}{(p+|m|)!}} P_p^m(\xi) \boldsymbol{M}_b^{pj} \cdot \boldsymbol{e}^{pm}.
\end{aligned}
\tag{22}
$$

8

1.1.2 Gyrokinetic Hermite-Laguerre expansion

Now we need to project equations 11 and 12 onto the Hermite-Laguerre basis, $\mathcal{C}_{ab}^{lk} = \mathcal{C}_{ab}^{lk}(\boldsymbol{k}, t)$. We focus first on the test component:

$$\mathcal{C}_{ab}^{Tlk} = \mathcal{C}_{ab}^{Tlk}(\boldsymbol{k}, t) = \sum_{p=0}^{\infty} \sum_{j=0}^{\infty} \sum_{m=-p}^{p} \frac{1}{\sigma_p^j} i^m \sqrt{\frac{\pi^{1/2} p!}{2^p (p-1/2)!}} \sqrt{\frac{(p-|m|)!}{(p+|m|)!}} \boldsymbol{M}_a^{pj} \cdot \boldsymbol{e}^{pm} \frac{\mathrm{I}_{abm}^{Tlkj}}{\sqrt{2^l l!}},$$

where

$$\mathrm{I}_{abm}^{Tlkpj} = \int \mathrm{d}v F_{Ma} v_{ab}^{Tpj} \, \mathrm{J}_m \left(\sqrt{x_a} b_a\right) P_p^m(\xi) H_l \left(s_{\|a}\right) L_k \left(x_a\right) \tag{23}$$

In the same way we have a similar expression for the field component $\mathcal{C}_{ab}^{Flk}$, replacing v_{ab}^{Tpj} by v_{ab}^{Fpj} in (3.23), and $\boldsymbol{M}_a^{pj}$ by $\boldsymbol{M}_b^{pj}$ in 23. Now we need to express the spherical harmonic particle moments $\boldsymbol{M}_a^{pj}$ through the gyromoments defined in 6 and in doing so we need to compute the velocity integral contained in 23.

As a first step, we transform the velocity-space integral in 18 to a phase-space integral, namely

$$\boldsymbol{M}_a^{pj}(\boldsymbol{r}) = \frac{1}{n_a} \int \mathrm{d}\boldsymbol{v} \int \mathrm{d}\boldsymbol{r}' \delta \left(\boldsymbol{r} - \boldsymbol{r}'\right) f_a \left(\boldsymbol{r}', \boldsymbol{v}\right) \boldsymbol{Y}^p \left(\boldsymbol{s}_a\right) L_j^{p+1/2} \left(s_a^2\right)$$

then using the coordinate transformation $\boldsymbol{r}' = \boldsymbol{r}'(\boldsymbol{R}, \mu, \theta) = \boldsymbol{R} + \boldsymbol{\rho}_a(\mu, \theta)$ we can write

$$\boldsymbol{M}_a^{pj}(\boldsymbol{r}) = \frac{1}{n_a} \int \mathrm{d}\theta \mathrm{d}\mu \mathrm{d}v_{\|} \mathrm{d}\boldsymbol{R} \frac{B}{m_a} \delta \left(\boldsymbol{r} - \boldsymbol{R} - \boldsymbol{\rho}_a\right) f_a \left(\boldsymbol{r}', \boldsymbol{v}\right) \boldsymbol{Y}^p \left(\boldsymbol{s}_a\right) L_j^{p+1/2} \left(s_a^2\right),$$

where $f_a \left(\boldsymbol{r}', \boldsymbol{v}\right) = f_a \left(\boldsymbol{r}'(\boldsymbol{R}, \mu, \theta), \boldsymbol{v} \left(\mu, v_{\|}, \theta\right)\right)$. Now we will express the perturbed particle distribution function $f_a \left(\boldsymbol{r}', \boldsymbol{v}\right)$ in terms of the perturbed gyrocentre distribution function, $g_a \left(\boldsymbol{R}, \mu, v_{\|}\right)$. Then, because of the scalar invariance of the total particle and gyrocentre distribution functions, we have

$$f_a \left(\boldsymbol{r}', \boldsymbol{v}\right) = g_a \left(\boldsymbol{R}, \mu, \boldsymbol{v}_{\|}\right) + F_{Ma} \left(\boldsymbol{R}, \mu, v_{\|}\right) - f_{Ma} \left(\boldsymbol{r}', \boldsymbol{v}\right). \tag{24}$$

Given that the gyrocenter coordinates $\left(\boldsymbol{R}, \mu, v_{\|}, \theta\right)$ arise from a perturbative coordinate transformation originating in the particle phase-space $(\boldsymbol{r}, \boldsymbol{v})$ through the Lie-transform perturbation method ([13]; [4]), any function F defined on $\left(\boldsymbol{R}, \mu, v_{\|}, \theta\right)$ can be expressed in terms of the functional form of a function f defined on $(\boldsymbol{r}, \boldsymbol{v})$, denoted as $f = \mathcal{T}F$.

In the specific scenario of $f = f_{Ma}$ and $F = F_{Ma}$, where $f_{Ma} = \mathcal{T}F_{Ma}$ in 24 and considering the leading-order approximation in $\epsilon \sim e\phi/T_e \ll 1$, it implies that the perturbed particle and gyrocenter distribution functions are linked by

$$f_a \left(\boldsymbol{r}', \boldsymbol{v}\right) = g_a \left(\boldsymbol{R}, \mu, v_{\|}\right) - \frac{q_a}{T_a} \left(\phi \left(\boldsymbol{r}'\right) - \langle\phi\rangle_R(\boldsymbol{R})\right) F_{Ma} \tag{25}$$

Moreover we recall that $\phi - \langle\phi\rangle_R \sim \left(k_\perp \rho_s\right)^2 e\phi/T_e$, the last term in 25 can be omitted in DK collision operators. Now we insert 25 in 18, and we get

$$M_a^{pj}(\boldsymbol{r}) = \boldsymbol{m}_a^{pj}(\boldsymbol{r}) + \sum_{i=1}^{2} \boldsymbol{m}_{a\phi i}^{pj}(\boldsymbol{r}) \tag{26}$$

with

$$\boldsymbol{m}_a^{pj}(\boldsymbol{r}) = \frac{1}{N_a} \int \mathrm{d}\theta \mathrm{d}\mu \mathrm{d}v_\parallel \frac{B}{m_a} \langle g_a \boldsymbol{Y}^p(\boldsymbol{s}_a) \rangle_{\boldsymbol{r}}^\dagger L_j^{p+1/2}(s_a^2),$$

$$\boldsymbol{m}_{a\phi 1}^{pj}(\boldsymbol{r}) = -\frac{q_a}{N_a T_a} \int \mathrm{d}\theta \mathrm{d}\mu \mathrm{d}v_\parallel \frac{B}{m_a} \left\langle \phi(\boldsymbol{R} + \boldsymbol{\rho}_a) \boldsymbol{Y}^p(\boldsymbol{s}_a) \right|_{\boldsymbol{r}}^\dagger L_j^{p+1/2}(s_a^2) F_{Ma}, \tag{27}$$

$$\boldsymbol{m}_{a\phi 2}^{pj}(\boldsymbol{r}) = \frac{q_a}{N_a T_a} \int \mathrm{d}\theta \mathrm{d}\mu \mathrm{d}v_\parallel \frac{B}{m_a} \langle\langle \phi \rangle_{\boldsymbol{R}}(\boldsymbol{R}) \boldsymbol{Y}^p(\boldsymbol{s}_a) \rangle_{\boldsymbol{r}}^\dagger L_j^{p+1/2}(s_a^2) F_{Ma},$$

where $\langle \xi \rangle_r^\dagger$ is the adjoint gyroaverage operator at the particle position r [1],

$$\langle \xi \rangle_r^\dagger = \int_0^{2\pi} \frac{\mathrm{d}\theta}{2\pi} \int \mathrm{d}\boldsymbol{R} \delta(\boldsymbol{R} + \boldsymbol{\rho}_a - \boldsymbol{r}) \xi(\boldsymbol{R}, v_\parallel, \mu, \theta)$$

defined over any gyrocentre phase-space function ξ.

Now, as stated before, we have to evaluate the velocity integral in $\boldsymbol{m}_a^{pj}$ defined 27. at first we compute $\langle g_a \boldsymbol{Y}^p(\boldsymbol{s}_a) \rangle_r^\dagger$ in Fourier space

$$\begin{aligned}
\boldsymbol{m}_a^{pj}(\boldsymbol{r}) &= \frac{1}{N_a} \int \mathrm{d}\boldsymbol{k} \int \mathrm{d}\theta \mathrm{d}\mu \mathrm{d}v_\parallel \frac{B}{m_a} g_a(\boldsymbol{k}, \mu, v_\parallel) \int_0^{2\pi} \frac{\mathrm{d}\theta'}{2\pi} \exp(-\boldsymbol{k} \cdot \boldsymbol{\rho}_a') \boldsymbol{Y}^p(\boldsymbol{s}_a') L_j^{p+1/2}(s_a^2) \mathrm{e}^{\mathrm{i}\boldsymbol{k}\cdot\boldsymbol{R}} \\
&= \frac{1}{N_a} \sum_{n=-\infty}^{\infty} (-\mathrm{i})^n \int \mathrm{d}\boldsymbol{k} \int \mathrm{d}\theta \mathrm{d}\mu \mathrm{d}v_\parallel \frac{B}{m_a} g_a(\boldsymbol{k}, \mu, v_\parallel) \mathrm{J}_n(b_a\sqrt{x_a}) \\
&\quad \times \int_0^{2\pi} \frac{\mathrm{d}\theta'}{2\pi} \mathrm{e}^{\mathrm{i}n\theta'} \boldsymbol{Y}^p(\boldsymbol{s}_a') L_j^{p+1/2}(s_a^2) \mathrm{e}^{\mathrm{i}\boldsymbol{k}\cdot\boldsymbol{R}}
\end{aligned} \tag{28}$$

where as before we use the Jacobi-Anger identity and we use ρ_a' and s_a' notation to indicate that these quantities have to be evaluated at θ'. As stated before, we can expand the Bessel functions into associated Laguerre polynomials and then evaluate the velocity integrals. Them we need a change of basis from the associated Legendre and Laguerre polynomials to the Hermite-Laguerre basis to express $\boldsymbol{m}_a^{pj}$ in terms of the gyromoments N_a^{pj}. This basis transformation can be found in [8] and has the form

$$\begin{aligned}
s_s^p P_p^m(\xi) L_j^{p+1/2}(s_s^2) &= \sum_{l=0}^{p+m+2j} \sum_{k=0}^{j+\lfloor (p+m)/2 \rfloor} T_{pjm}^{lk} H_l(s_{\parallel s}) L_k(x_s) x_s^{m/2}, \\
H_l(s_{\parallel s}) L_k(x_s) x_s^{m/2} &= \sum_{p=0}^{l+m+2k} \sum_{j=0}^{k+\lfloor (l+m)/2 \rfloor} (T^{-1})_{lk}^{pjm} s_s^p P_p^m(\xi) L_j^{p+1/2}(s_s^2),
\end{aligned} \tag{29}$$

where the closed analytical expression of the coefficients T_{pjm}^{lk} is in [8], and the coefficients $(T^{-1})_{lk}^{pjm}$ of the inverse basis transformation, are given by

$$\left(T^{-1}\right)_{lk}^{pjm} = \frac{\sqrt{\pi}2^l l j!(p+1/2)}{(j+p+1/2)!}\frac{(p-m)!}{(p+m)!} \times \sum_{k'=0}^{\min(j+\lfloor(p+m)/2\rfloor,m+k)} T_{pjm}^{lk'}d_{0kk'}^m [l \le p+m+2j]$$

with [.] the Iverson bracket, defined by $[A] = 1$ if A is true, and 0 otherwise. Then using the basis transformation shown above we can express $\boldsymbol{m}_a^{pj}$ in function of the gyromoments

$$\boldsymbol{m}_a^{pj} = \boldsymbol{m}_a^{pj}(\boldsymbol{k}) = \sqrt{\frac{\pi^{1/2}p!}{2^p(p-1/2)!}}\sum_{m=-p}^{p}(-\mathbf{i})^m\sqrt{\frac{(p-|m|)!}{(p+|m|)!}}\mathcal{M}_a^{pjm}\boldsymbol{e}^{pm}$$

where

$$\mathcal{M}_a^{pjm} = \sum_{g=0}^{p+|m|+2j}\sum_{h=0}^{j+\lfloor(p+|m|)/2\rfloor}\sum_{n=0}^{\infty}\sum_{s_1=0}^{n+|m|+h}d_{nhs_1}^{|m|}T_{pj|m|}^{gh}\frac{n!\sqrt{2^g g!}}{(n+|m|)!}\left(\frac{b_a}{2}\right)^{|m|}\mathcal{K}_n\left(b_a\right)N_a^{gs_1}. \quad (30)$$

Moreover, the numerical coefficients $d_{nks_1}^{|m|}$ arise from the product between Laguerre and associated Laguerre polynomials,

$$L_n^m(x)L_k(x)x^m = \sum_{s=0}^{n+m+k}d_{nks}^m L_s(x)$$

and an analytical expression for them is [8],

$$d_{nks}^m = \sum_{n_1=0}^{n}\sum_{k_1=0}^{k}\sum_{s_1=0}^{s}L_{kk_1}^{-1/2}L_{nn_1}^{m-1/2}L_{ss_1}^{-1/2}\left(n_1+k_1+s_1+m\right)!$$

with the coefficients L_{jl}^p defined in 15.

For the polarization terms $\boldsymbol{m}_{a\phi1}^{pj}$ and $\boldsymbol{m}_{a\phi2}^{pj}$ defined in 27 a full derivation can be found in [1]: the strategy is the same of the coefficient $\boldsymbol{m}_a^{pj}$. After carrying out similar computations for the polarization terms we finally have a Hermite-Laguerre expansion of the collision operator. The Hermite-Laguerre expansion of the linearized GK Coulomb collision operator $\mathcal{C}_{ab}^{lk} = \mathcal{C}_{ab}^{lk}(\boldsymbol{k},t)$ reads

$$\mathcal{C}_{ab}^{lk} = \mathcal{C}_{ab0}^{Tlk} + \mathcal{C}_{ab0}^{Flk} + \sum_{i=1}^{2}\left(\mathcal{C}_{ab\phi i}^{Tlk} + \mathcal{C}_{ab\phi i}^{Flk}\right)$$

with the Hermite-Laguerre expansion of the test and field components, $\mathcal{C}_{ab0}^{Tlk}$ and $\mathcal{C}_{ab0}^{Flk}$, given by

11

$$
\begin{aligned}
\mathcal{C}_{ab0}^{Tlk} =& \sum_{p=0}^{\infty}\sum_{j=0}^{\infty}\sum_{n=0}^{\infty}\sum_{f=0}^{k+n}\sum_{m=0}^{p}\sum_{t=0}^{f+\lfloor(l+m)/2\rfloor}\frac{a_m}{\sigma_p^j}\frac{2^p(p!)^2}{(2p)!}\frac{\bar{d}_{nkf}^m}{(2p+1)} \\
&\times \frac{(T^{-1})_{lf}^{ptm}}{\sqrt{2^l l!}}\frac{n!\mathcal{K}_n(b_a)}{(n+m)!}\left(\frac{b_a}{2}\right)^m \mathcal{M}_a^{pjm}\bar{v}_{ab}^{Tpjt}[p\leq l+m+2f], \\
\mathcal{C}_{ab0}^{Flk} =& \sum_{p=0}^{\infty}\sum_{j=0}^{\infty}\sum_{n=0}^{\infty}\sum_{f=0}^{k+n}\sum_{m=0}^{p}\sum_{t=0}^{f+\lfloor(l+m)/2\rfloor}\frac{a_m}{\sigma_p^j}\frac{2^p(p!)^2}{(2p)!}\frac{\bar{d}_{nkf}^m}{(2p+1)} \\
&\times \frac{(T^{-1})_{lf}^{ptm}}{\sqrt{2^l l!}}\frac{n!\mathcal{K}_n(b_a)}{(n+m)!}\left(\frac{b_a}{2}\right)^m \mathcal{M}_b^{pjm}\,\bar{v}_{ab}^{Fpjt}[p\leq l+m+2f],
\end{aligned}
\tag{31}
$$

where $\bar{v}_{ab}^{Tpjt}$ and $\bar{v}_{ab}^{Fpjt}$ are the velocity integrated speed functions and have the form

$$
\bar{v}_{ab}^{Tpjt} = \sum_{d=0}^{t}L_{td}^p\bar{\nu}_{*ab}^{Tpjd},
$$

$$
\bar{v}_{ab}^{Fpjt} = \sum_{d=0}^{t}L_{td}^p\bar{v}_{*ab}^{Fpjd},
$$

where $\bar{v}_{*ab}^{Tpjd} = \int d\boldsymbol{v}s_a^{p+2d}v_{ab}^{Tpj}F_{Ma}$ and $\bar{v}_{*ab}^{Fpjd} = \int d\boldsymbol{v}s_a^{p+2d}v_{ab}^{Fpj}F_{Ma}$. A closed analytical expressions for $\bar{v}_{ab*}^{Tpjd}$ and $\bar{v}_{ab*}^{Fpjd}$ can be found in the Appendix A of [1]. The remaining coefficients of 31 can be found in [1].

1.1.3 Drift-kinetic limit of Coulomb collision operator

Now we can take the drift kinetic limit of the GK linearized Coulomb collision operator: this can be computed by neglecting the FLR effects in the test and field components as well as the polarization terms. For instance, in the zero gyroradius limit we see that to $f_a = g_a$. Moreover, the gyromoment expansion of the spherical harmonic particle moments, $\boldsymbol{M}_a^{pj}$ in 26 reduces to

$$
\boldsymbol{M}_a^{pj} = \sqrt{\frac{\pi^{1/2}p!}{2^p(p-1/2)!}}\mathcal{M}_a^{pj}\boldsymbol{e}^{p0}
$$

where

$$
\mathcal{M}_a^{pj} = \sum_{g=0}^{p+2j}\sum_{h=0}^{j+\lfloor p/2\rfloor}T_{pj}^{gh}\sqrt{2^g g!}N_a^{gh}
\tag{32}
$$

If we then also neglect finite Larmor radius effects in 22, such that $\langle C_{ab}(\boldsymbol{r},\boldsymbol{v})\rangle_R \simeq \langle C_{ab}(\boldsymbol{R},\boldsymbol{v})\rangle_R$, and we project the resulting expression onto the Hermite-Laguerre basis, we obtain the Hermite-Laguerre expansion of the linearized DK Coulomb collision operator :

$$\mathcal{C}_{ab}^{Tlk} = \sum_{j=0}^{\infty} \sum_{p=0}^{l+2k} \sum_{t=0}^{k+\lfloor l/2 \rfloor} \sum_{d=0}^{t} \frac{2^p(p!)^2}{(2p)!\sigma_p^j} \frac{L_{td}^p}{(2p+1)} \frac{(T^{-1})_{lk}^{pt}}{\sqrt{2^l l!}} \mathcal{M}_a^{pj} \bar{v}_{*ab}^{Tpjd},$$
$$\mathcal{C}_{ab}^{Flk} = \sum_{j=0}^{\infty} \sum_{p=0}^{l+2k} \sum_{t=0}^{k+\lfloor l/2 \rfloor} \sum_{d=0}^{t} \frac{2^p(p!)^2}{(2p)!\sigma_p^j} \frac{L_{td}^p}{(2p+1)} \frac{(T^{-1})_{lk}^{pt}}{\sqrt{2^l l!}} \mathcal{M}_b^{pj} \bar{v}_{*ab}^{Fpjd},$$

(33)

If we insert 32 into 33 we obtain:

$$\mathcal{C}_{ab}^{Tlk} = \sum_{j=0}^{\infty} \sum_{p=0}^{l+2k} \sum_{t=0}^{k+\lfloor l/2 \rfloor} \sum_{d=0}^{t} \sum_{g=0}^{p+2j} \sum_{h=0}^{j+\lfloor p/2 \rfloor} \frac{2^p(p!)^2}{(2p)!\sigma_p^j} \frac{L_{td}^p}{(2p+1)} \frac{(T^{-1})_{lk}^{pt}}{\sqrt{2^l l!}} T_{pj}^{gh} \sqrt{2^g g!} N_a^{gh} \bar{v}_{*ab}^{Tpjd},$$
$$\mathcal{C}_{ab}^{Flk} = \sum_{j=0}^{\infty} \sum_{p=0}^{l+2k} \sum_{t=0}^{k+\lfloor l/2 \rfloor} \sum_{d=0}^{t} \sum_{g=0}^{p+2j} \sum_{h=0}^{j+\lfloor p/2 \rfloor} \frac{2^p(p!)^2}{(2p)!\sigma_p^j} \frac{L_{td}^p}{(2p+1)} \frac{(T^{-1})_{lk}^{pt}}{\sqrt{2^l l!}} T_{pj}^{gh} \sqrt{2^g g!} N_b^{gh} \bar{v}_{*ab}^{Fpjd},$$

Using now a cutoff index j_{max} for the j index and the Iverson brackets we can rearrange the terms to obtain:

$$\mathcal{C}_{ab}^{Tlk} = \sum_{g=0}^{\infty} \sum_{h=0}^{\infty} \sum_{j=0}^{j_{max}} \sum_{p=0}^{l+2k} \sum_{t=0}^{k+\lfloor l/2 \rfloor} \sum_{d=0}^{t} \frac{2^p(p!)^2}{(2p)!\sigma_p^j} \frac{L_{td}^p}{(2p+1)} \frac{(T^{-1})_{lk}^{pt}}{\sqrt{2^l l!}} T_{pj}^{gh} \sqrt{2^g g!} N_a^{gh} \bar{v}_{*ab}^{Tpjd} [g \le p+2j] \times [h \le j+\lfloor p/2 \rfloor]$$
$$\mathcal{C}_{ab}^{Flk} = \sum_{g=0}^{\infty} \sum_{h=0}^{\infty} \sum_{j=0}^{j_{max}} \sum_{p=0}^{l+2k} \sum_{t=0}^{k+\lfloor l/2 \rfloor} \sum_{d=0}^{t} \frac{2^p(p!)^2}{(2p)!\sigma_p^j} \frac{L_{td}^p}{(2p+1)} \frac{(T^{-1})_{lk}^{pt}}{\sqrt{2^l l!}} T_{pj}^{gh} \sqrt{2^g g!} N_b^{gh} \bar{v}_{*ab}^{Fpjd} [g \le p+2j] \times [h \le j+\lfloor p/2 \rfloor],$$

Now we can easily see that this can be represented in a matricial form introducing the matrices

$$A_{gh}^{Tlk} = \sum_{j=0}^{j_{max}} \sum_{p=0}^{l+2k} \sum_{t=0}^{k+\lfloor l/2 \rfloor} \sum_{d=0}^{t} \frac{2^p(p!)^2}{(2p)!\sigma_p^j} \frac{L_{td}^p}{(2p+1)} \frac{(T^{-1})_{lk}^{pt}}{\sqrt{2^l l!}} T_{pj}^{gh} \sqrt{2^g g!} \bar{v}_{*ab}^{Tpjd} [g \le p+2j] \times [h \le j+\lfloor p/2 \rfloor]$$

$$A_{gh}^{Flk} = \sum_{j=0}^{j_{max}} \sum_{p=0}^{l+2k} \sum_{t=0}^{k+\lfloor l/2 \rfloor} \sum_{d=0}^{t} \frac{2^p(p!)^2}{(2p)!\sigma_p^j} \frac{L_{td}^p}{(2p+1)} \frac{(T^{-1})_{lk}^{pt}}{\sqrt{2^l l!}} T_{pj}^{gh} \sqrt{2^g g!} \bar{v}_{*ab}^{Fpjd} [g \le p+2j] \times [h \le j+\lfloor p/2 \rfloor]$$

We call A_{gh}^{lk} the moments matrix. In this way we see that the computational complexity of solving 7 for all the gyromoments is $O(N^2)$ in the number of gyromoments since we have

$$\mathcal{C}_{ab}^{Tlk} = \sum_{g=0}^{p_{max}} \sum_{h=0}^{j_{max}} A_{gh}^{Tlk} N_a^{gh}$$
$$\mathcal{C}_{ab}^{Flk} = \sum_{g=0}^{p_{max}} \sum_{h=0}^{j_{max}} A_{gh}^{Flk} N_b^{gh}$$

(34)

.

where j_{max} and p_{max} are cut-off indices in the Hermite-Laguerre space.

2   Matricial patterns and filters

In the previous section, we briefly introduced the gyromoment approach, and we observed that the final expression of the collision operator can be represented in a matricial form, giving a quadratic computational cost with respect to the number of gyromoments for the solution of 7. We recall that the gyromoments are defined as 6. However, the matrices of this representation are sparse and present peculiar patterns. The idea is then to design a filter for those matrices in order to extract all the meaningful information and avoid the computation of matrix elements that are not meaningful for our purpose. After testing the filters within the matricial form, we will test the performance of those filters in simulating the electron plasma wave. At first, we will analyze the performance of the filters for the self-interaction term C_{ee}^{lk}; then we will move on to the analysis of the electron-ion interaction term C_{ei}^{lk}. We start by analyzing the self-interaction term because, in a real scenario, electron-electron interactions have more wights than electron-ion interactions due to the mass difference. Moreover, to have a finite moments matrix, we will set a threshold for the number of moments in the Hermite-Laguerre space that is chosen according to the convergence of the simulation. The matrix will be a square matrix of dimension $(p_{max} + 1) \times (j_{max} + 1)$ where p_{max} and j_{max} are the cut-off indices for the Hermite and Laguerre moments'order, respectively. Finally, we recall that in this matricial representation using the cut-off indices for the Hermite-Laguerre basis, the moments vector $\mathbf{N}$ will have the following structure:

$$\mathbf{N} = \begin{bmatrix} N^{00} \\ N^{01} \\ \vdots \\ N^{0j} \\ N^{10} \\ N^{11} \\ \vdots \\ N^{1j} \\ \vdots \\ N^{pj} \end{bmatrix}$$

2.1   Matricial Patterns

As previously stated, we will start considering the C_{ee}^{lk} term (note that for this term, the test and field part are the same due to the symmetry of the operator): looking at figure 1 we observe that there is no correlation between even and odd moments in the Hermite space, i.e. we only need to compute the following products:

$$\sum_{g=0}^{p_{max}} \sum_{h=0}^{j_{max}} A_{2g,h}^{lk} N^{2g,h}$$

for even moments and

$$\sum_{g=0}^{p_{max}} \sum_{h=0}^{j_{max}} A_{2g+1,h}^{lk} N^{2g+1,h}$$
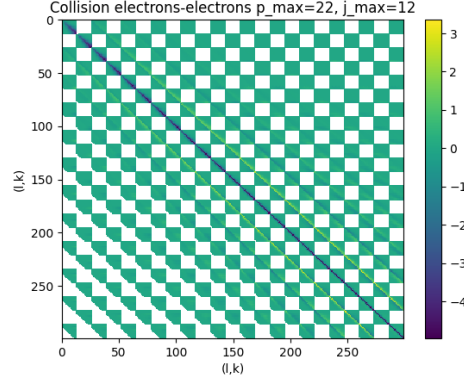
Figure 1: Plot of the electron-electron moments matrix. In this plot, the white entries have 0 value. One can observe that we do not have any correlation between odd and even Hermite moments. Furthermore, we notice a particular pattern: the most relevant entries are distributed in a multi-diagonal-like structure.

for odd moments.

Moreover, we notice a nice structure: the matrix, as previously said, is sparse, and the most relevant entries are distributed in a multi-diagonal-like structure. We can also observe that the left-down corner breaks the symmetry of the matrix; this phenomenon is probably due to numerical errors, but it does not affect the simulation since those entries will have values with a very small magnitude (they should be equal to the ones in the right-up corner). Now that we have seen that the main entries are disposed in this particular pattern, we need a way of visualizing better how to extract the information, neglecting all the 'noise' and thus using the sparsity of A_{gh}^{lk}. To do so, we introduce a visualization of the matrix that we call 'diagonal view': this visualization is nothing but plotting the absolute magnitude of the moments matrix entries of each of the equations 7, i.e. each row (the scalar product between each row of the matrix and the moments vector gives the right-hand side of one of the components of the system of equations 7, so each row is associated with an equation), in function of the distance from the main diagonal. In doing so, we are able to obtain a nice picture of the structure of the matrix. In figure2 we can see that, from this point of view, the relevant information contained inside the entries is distributed according to a specific law; indeed, we notice that the relevant entries have the same pattern for all the rows of the matrix. Specifically, the peaks follow a precise pattern, and their position is always a multiple of $2(j_{max} + 1)$. It is important to notice that we observe significant values only near to the peaks. We are then able to create a filter that will isolate all the main information.

Now we compute the contour line of the diagonal view and an 'average' to obtain the average importance of each moment among all the equations. To do so, we first compute a 'contour matrix' that is nothing but a matrix with twice the columns of the original moments matrix and created by shifting all the rows in order to have the diagonal elements aligned in the middle (we then take the absolute value). Then we use two different metrics to create different visualizations: in the first approach, we compute the maximum of each column tracing the contour line of the diagonal view, and, in the second approach, we compute an average value. As one can see in figure 3, we are interested in computing the average because,

15
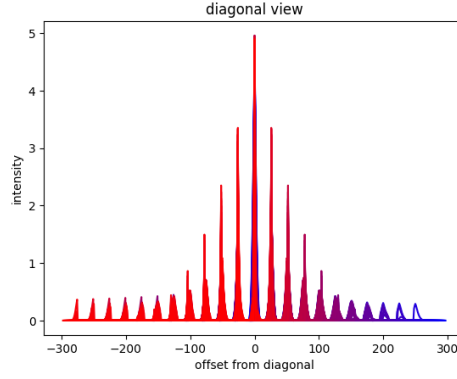
Figure 2: Diagonal view of the moments matrix for the electron-electron interaction. We use a color gradient going down the main diagonal to see if the pattern changes depending on the row: overall, we can see that all the rows follow the same pattern. Moreover, we have almost the same number of peaks to the right and to the left of the main peak; indeed, we have one peak less on the right of the main peak, and this is due to the previous numerical problem of the computation of the left-down corner entries.
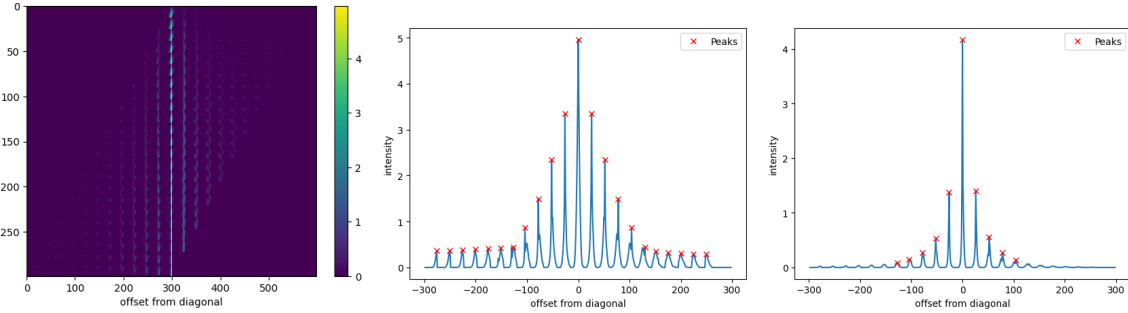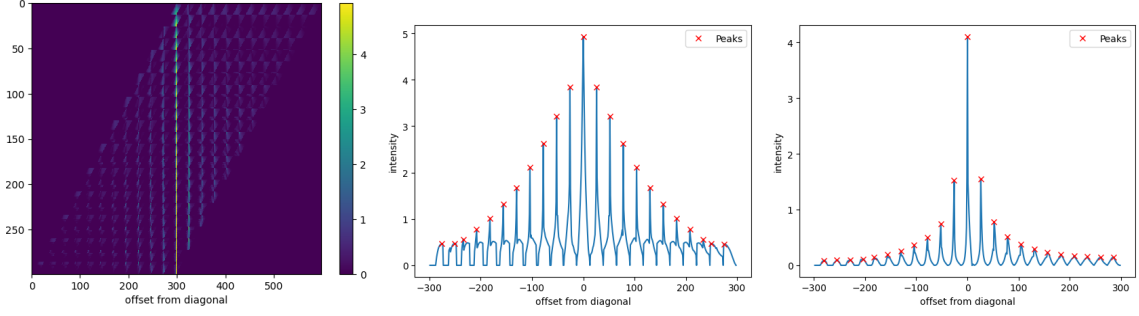

Figure 3: Plot of the contour matrix (left) [2], contour line of the diagonal view (right) and average diagonal view (bottom).

in this way, we see that only a small number of peaks have often a large importance in the solution of our system.

Another interesting pattern to be noticed is that going down the matrix, i.e. increasing the row index, the value of the peaks changes following a precise scheme: the main peak increases rapidly and then stabilizes around a value ~ 5; the other peaks grow less than the main one, but they show too a periodic behavior

---

[2]the y axis in the contour matrix plot stands for the row-index: we were not able to label it in the plot due to a bug for non square matrices in pyplot. The same holds for future contour matrices plots.
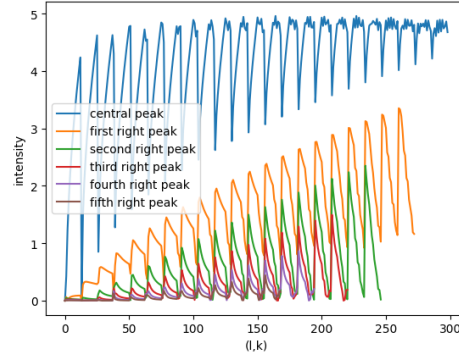
Figure 4: Plot of the periodic behaviour of the peaks' value

We observed the same patterns also using different perpendicular wavenumbers (here we have shown all the plots using the perpendicular wavenumber $k = 0$).

After having analyzed the electron-electron part, it is interesting to inspect the electron-ion part: in this case, the only matrix that presents a similar structure is the test part (figure 5). As we can see, the diagonal view presents a slightly different pattern. In addition, we can test how the mass ratio between different species a, b influences the structure of the matrix. In the presented example, we are using the real mass ratio between electrons and ions $\sigma = 5.45e - 04$. The mass ratios we are going to use are $\sigma_0 = 1 \quad \sigma_1 = 1.53e - 01 \quad \sigma_2 = 2.33e - 02 \quad \sigma_3 = 3.57e - 03 \quad \sigma_4 = 5.45e - 04$. When plotting the magnitude of the peaks as a function of the mass ratio, we see that the height of the peaks is a decreasing function of the mass ratio. Moreover, the peaks that differ the most change when using the average diagonal view, as one can see from figures 8 and 9. These metrics suggest that using smaller mass ratios will make our filters less effective since we need to take into account more peaks and the diagonal view presents less empty zones.
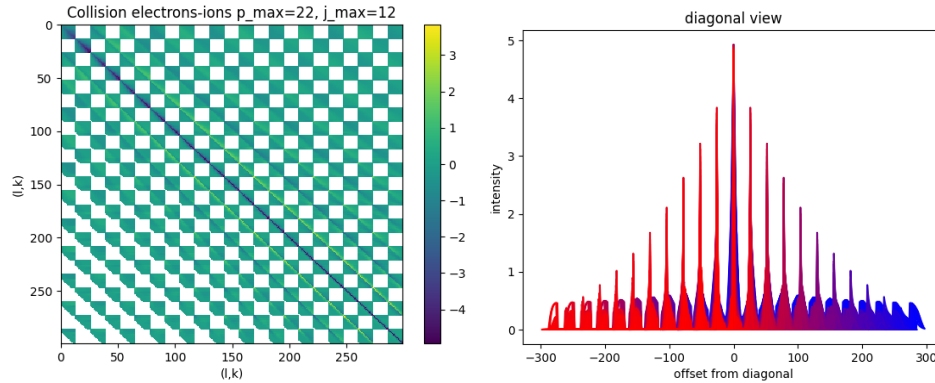
Figure 5: Plot of electron-ion moments matrix and its diagonal view.

Figure 6: Plot of the contour matrix (left), contour line of the diagonal view (right) and average diagonal view (bottom) of the electron-ion test moments matrix.
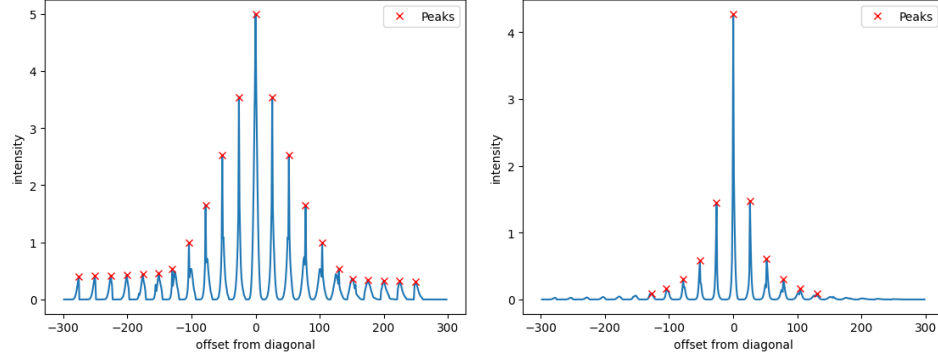
Figure 7: Plot of electron-ion diagonal view for mass ratio $\sigma = 1$. We observe a meaningful difference between the real mass ratio $\sigma = 5.45e - 04$
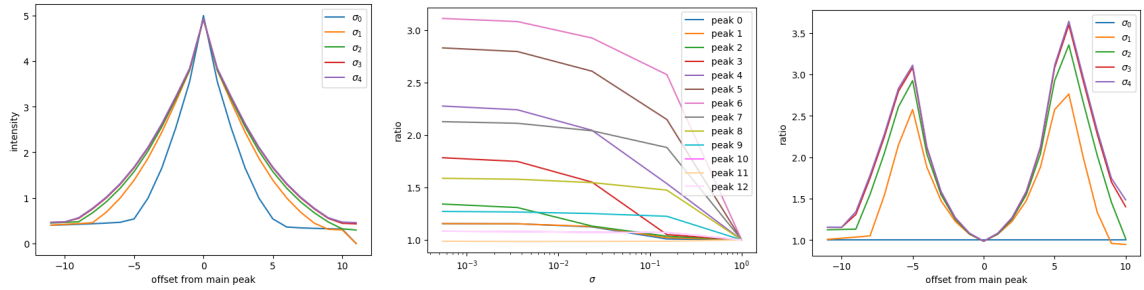
Figure 8: Effect of the mass ratio on the peaks of the diagonal view. In the central figure, we only plot half of the peaks plus the central one because of the symmetric nature of the matrix.
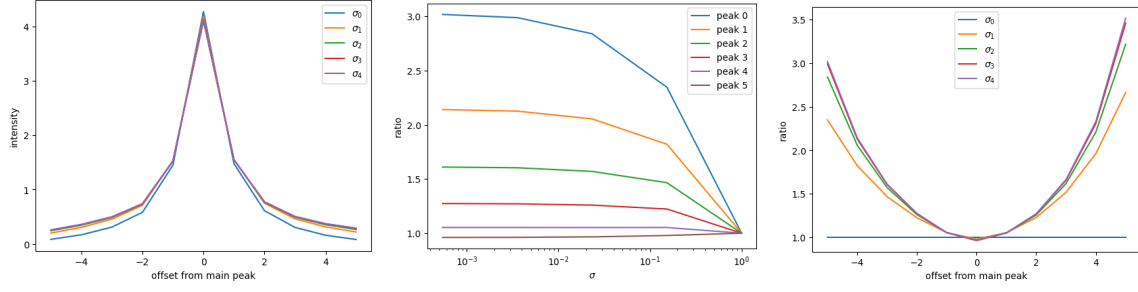
Figure 9: Effect of the mass ratio on the peaks of the average diagonal view. In this case we have less peaks because of the nature of the average diagonal view(less peaks appear in this case).

2.2 Filters

After having investigated different patterns in the previous matrices, it is time to try to extract the information inside them to see if we can reduce the computational cost. To do so, we get inspired by the diagonal view of the matrices: figure 2 is telling us that we need to consider entries that are not too far from the peaks. Moreover, since the height of the peaks reduces going far from the central peak, we can take into account only some of them; this is doable because the position of the peaks is a multiple of $2(j_{max}+1)$ and thus we know where they are located. We can then have an analytical formulation for these two approximations:

$$\mathbf{\Phi_{glob}}(A_{ij}, m_1) = A_{ij}[|i-j| \le (j_{max}+1) + m_1 \times 2(j_{max}+1)]$$
$$\mathbf{\Phi_{peak}}(A_{ij}, m_2) = A_{ij}[(|i-j| \bmod 2(j_{max}+1)) \le m_2] + A_{ij}[(|i-j| \bmod 2(j_{max}+1)) \ge 2(j_{max}+1)) - m_2]$$
(35)

where $m_1, m_2 \in \mathbb{R}$ and A_{ij} is a square matrix (we are using the Iverson brackets as before). $\mathbf{\Phi_{glob}}$ and $\mathbf{\Phi_{peak}}$ are called respectively global filter and peak filter. As suggested by their names, the global filters will take into account only the first m_1 peaks to the left and m_1 peaks to the right of the main peak; the peak filter instead will take into account only the entries that have a distance from the peaks less than m_2. To see explicitly the actions of these two filters, we have a look at figures 10 and 11: we observe that the filters are doing what we want, extracting the multi-diagonal structure of the matrix and suppressing the peaks that are not meaningful. Now that we have a correct and generalizable formulation for the filters, we need to put them to the test using some metrics. The first test we will perform will be to see how different matrix vector products are using these approximations. To do so, we generate random vectors, compute the matrix vector products with the full matrix and the approximated matrices, and we compute an empirical average of the relative errors obtained from the matrix-vector products. Looking at figures 12 and 13 we notice that the filters are working properly and manage to obtain good performance compared to the number of nonzero entries they keep. It is also important to notice that these two filters will give an approximation of the form:

$$\mathbf{C}_{ee}^{lk} = \alpha_0 N^{l-2m1,k-m2} + \cdots + \alpha_{4m_1} N^{l+2m_1,k-m2} + \cdots + \alpha_{4m_1+1} N^{l-m1,k-m2+1}$$
$$+ \cdots + \alpha_{8m_1} N^{l+m1,k-m2+1} + \cdots + \alpha_{8m_1 m_2} N^{l+m1,k+m2}$$
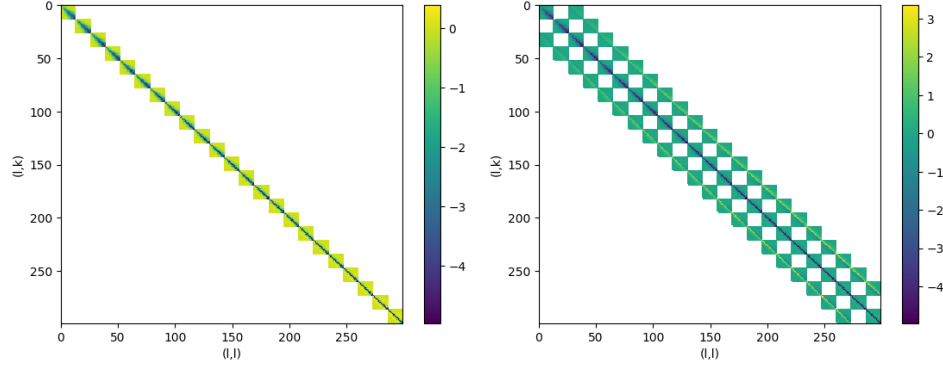(36)

19

Figure 10: Action of the global filter on the previous electron-electron moments matrix. We use first $m_1 = 0$ (left) $m_1 = 1$ (right)
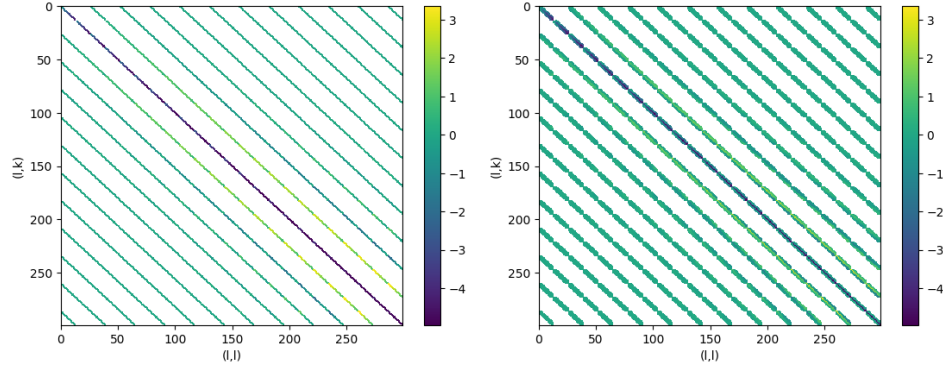

Figure 11: Action of the peak filter on the previous electron-electron moments matrix. We use first $m_2 = 0$ (left) $m_2 = 2$ (right)

where the numerical coefficients α_i are entries of the moments matrix (with matching indices to the moments' indices). With this formulation, we see that in the end we only need $(4m_1 + 1)(2m_2 + 1)$ coefficients. Actually, we could add some constraints to slightly reduce the number of coefficients; namely, we could exploit the total absence of correlation between odd and even Hermite moments to halve the number of Hermite moments. In this way, we get a complexity of $O(4m_1 m_2 N)$(we could apply the same reasoning to the peak filter, but in this case we will not get a simple simplification as the one obtained in the global filter case; in addition, the advantage will be smaller since the peak filter focuses on the Laguerre space only. It is important to notice that applying these filters gives us a Dougherty-like structure of the collision operator, and we end up with an approximation whose computational complexity is less than quadratic; in fact, in the end, the computational complexity applying these two filters will be $O(4m_1 m_2 N)$ where N is the number of gyromoments used. Moreover, if we use the fact that we could split the matrix into two parts, one for the even Hermite moments and one for the odd ones, we could further simplify the peak filter to obtain $O(\alpha m_1 m_2 N)$ with $\alpha < 4$.
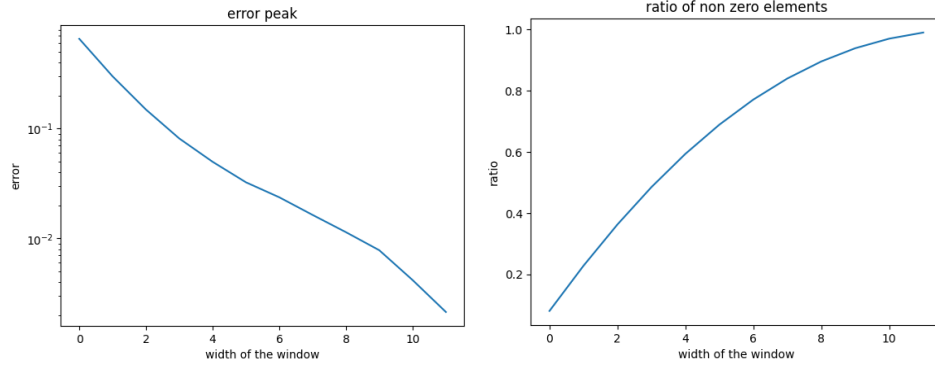
Figure 12: Error of the global filter in function of the number of peaks (the actual number of peaks is twice the one indicated on the x-axis since we take a symmetric window around the main peak).
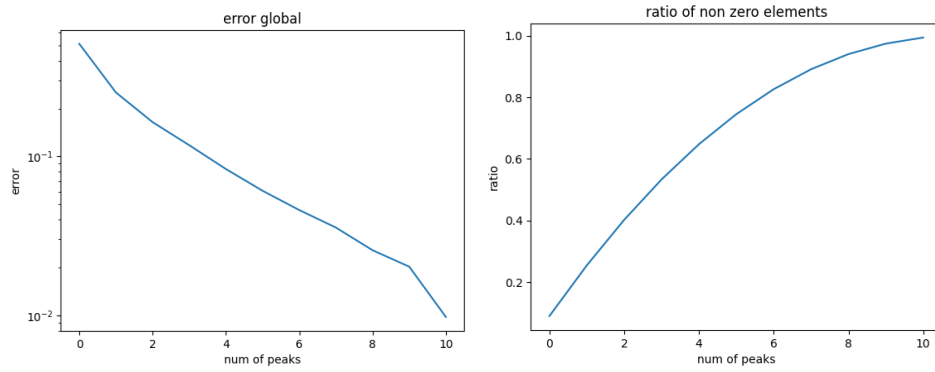

Figure 13: Error of the peak filter in function of the width of the peak window.

Now we can do the same test on the electron-ion moments matrix (test part): in this case, as previously suggested by the plots of the diagonal view using different mass ratios, we see that the approximation using the real mass ratio is less effective than the one using a mass ratio $\sigma = 1$. Indeed, in figure 14 we notice that even if the behavior of the error is similar in the logarithmic scale, we do not recover the same accuracy, neither with the peak nor the global window. This is due to the fact that using the real mass ratio introduces different effects in the diagonal view. Indeed, as shown in figures 6 and 7 the diagonal view of the real mass-ratio matrix presents higher peaks and less empty zones between neighboring peaks. However, even if the performance worsens, we can say that the filters are properly working. Now that everything is correctly set up, we need to test the performance of the filtered matrices in real plasma simulations.
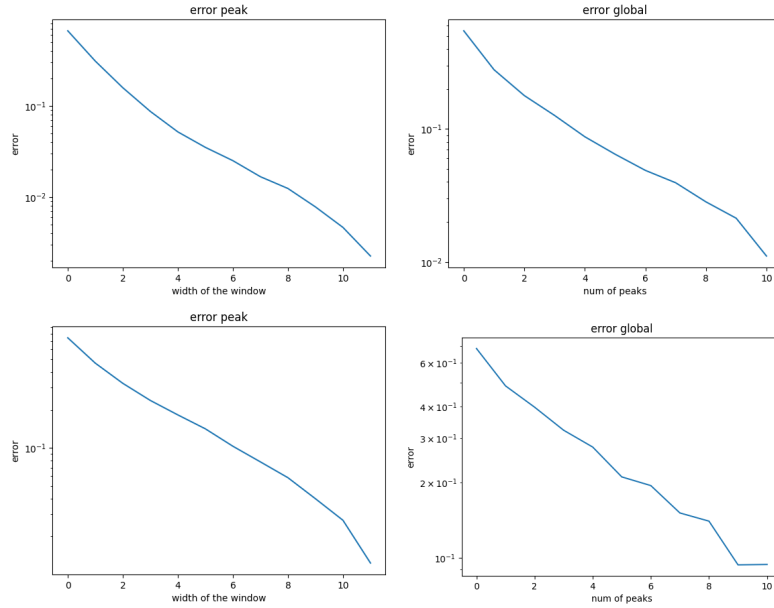
Figure 14: Error of the global and the peak filter in function of the width of the peak window. The first two figure are computed using $\sigma = 1$ whereas the bottom one are computed using the real electron-ion mass ratio.

3 Numerical simulations

As we previously noticed, the filters are working properly, giving us good approximations for the matrices with respect to the previous matrix-vector product metric. Now it is time to put them to the test in a real plasma simulation. To do so, we will use the Electron Plasma Wave model (EPW), changing the left-hand side of 1:

$$\frac{\partial f_a}{\partial t} + v_z \frac{\partial f_a}{\partial z} + \frac{\partial \phi}{\partial z} \frac{\partial f_a}{\partial v_z} = \sum_b C_{ab}$$

$$\frac{\partial^2 \phi}{\partial z^2} = \frac{1}{N_0} \int f_a \, d\boldsymbol{v} - 1. \tag{37}$$

More details about this equation can be found in [14]. Specifically, we will first perform a simulation with the full collision operator; then we will perform simulations with the filtered matrices, and we will compare them through some metrics as a function of the parameters m_1 and m_2. The metrics are based on the electrostatic potential $\Phi(t)$: the electrostatic potential presents an exponential decay within two different regimes. The first regime is characterized by an oscillatory behavior that is exponentially damped; the second regime, instead, does not present any oscillation. For our metrics, we will focus on this second regime, also called the entropy mode, and we will compare the exponential decay rate, also called the damping rate, and the relative average error of the electrostatic potential in this regime. We take an average of the error in the last points of the electrostatic potential because we see that in some simulations the approximated matrices give origin to the oscillation of the electrostatic potential around the true one, and thus an average error of the last points is a more reasonable estimate. The following simulations are performed with collision frequency $\nu/\omega_p = 0.23$ and using the real mass ratio of electrons and ions.

At first, we will test the performance of the filters for the electron-electron Coulomb matrix; in this case, we model the electron-ion interaction with the pitch-angle collision operator that is obtained by the expansion of the Coulomb collision operator in the limit of the small mass ratio[8] :

$$C_{ei}^{pj} = 2\pi \sum_{l=0}^{p+2j} \sum_{k=0}^{j+\lfloor p/2 \rfloor} \frac{\left(\mathrm{T}^{-1}\right)_{pj}^{lk0} v_{Te}^3}{\sqrt{2^p p!}} I_{ei}^{lk} \tag{38}$$

where the coefficients $\left(\mathrm{T}^{-1}\right)_{pj}^{lk0}$ and I_{ei}^{lk} can be found in [8]. At first, we test the global filter: to have convergence of the simulation, we need at least $m_1 \geq 3$. As one can observe in figure 15 the approximation works really well and even with $m_1 = 4$, that is using only up to 9 Hermite moments for each equation (we say 'up to' because if we are considering C_{ee}^{lk} then we will need Hermite moments with index from $l - 4$ to $l + 4$ but if $l = 0$ then we clearly see that we do not have any moments for negative indices; the same holds when l is equal to the maximum Hermite index p_{max}) we get an error of $5e - 03$ for the relative average error of the electrostatic potential and $1e - 03$ for the relative error in the damping rate.

Now that we have seen that the global filter is working very well, we test the peak filter. As one can see from figure 16 the peak filter is working very well too: indeed, we can see that, even if we need $m_2 > 3$ not to have divergent behavior within our time horizon (however, we could anyway obtain the damping rate by cutting the diverging part in the end), for $m_2 = 4$

we have an average relative error $\sim 1e - 03$ and a relative error for the damping rate of the entropy mode $\sim e - 04$. Now we check how the approximations work by changing the collision frequency: First, we test the global filter and the peak filter. From figure 17 we can see that the relative error of the damping rate of the entropy mode obtained at different collision frequencies through different m_1 is stable with respect to the collision frequency. Moreover, looking at figure 18 we can see that even the peak approximations are stable in the relative error for the damping rate of the entropy mode with respect to different collision frequencies. Now that we have tested the two filters separately, we test them together using the same value for both of them to see their combined performance: Looking at figure 19 we see that even with $m_1 = m_2 = 4$ we get really good performance for both the average relative error for the electrostatic potential and the relative error in the damping rate for the entropy mode. Finally, we tried to create a map to estimate the relative error in the damping rate as a function of m_1 and m_2 using the least squares method: First, we tried to interpolate the different errors with a plane with poor results; then, we tried to do the same thing, adding nonlinear and quadratic terms. However, with the best interpolation, shown in figure 20, we obtained a lack of fit equal to 18%, which is not enough to be confident on such a map. Overall, we can say that the performance of the different filters is really good for the linear Coulomb C_{ee} collision operator in the drift kinetic limit.

Now we test the electron ion test part using the full C_{ee} without any approximation (the other parameters of the simulation, for example, the collision frequency, are the same as before): previously, we observed that the diagonal view and the matricial error test, respectively in figures 5 and 14, suggest that this approximation is working worse in the case of the electron-ion part. Unfortunately, the suggestion is true: as one can observe by looking at figure 21 the performance of the peak filter is not good at all. However, we think that there could be an issue in the simulation itself since the difference between the approximation using $m_2 = 11$ (i.e. almost all the Laguerre moments) and the true simulation is a bit too far (this is also suggested by the fact that we did several tests using submatrices with 11 (or less) out of the 12 Laguerre moments of the original matrix getting, for this submatrices, an electrostatic potential evolution far from the one obtained using all the 12 moments, indicating that maybe we would need more Laguerre moments to have convergence to the true value.). The performance of the global filter is slightly worse and we further observe that the performances of both filters slightly improves considering mass ratios $\sigma \to 1$.
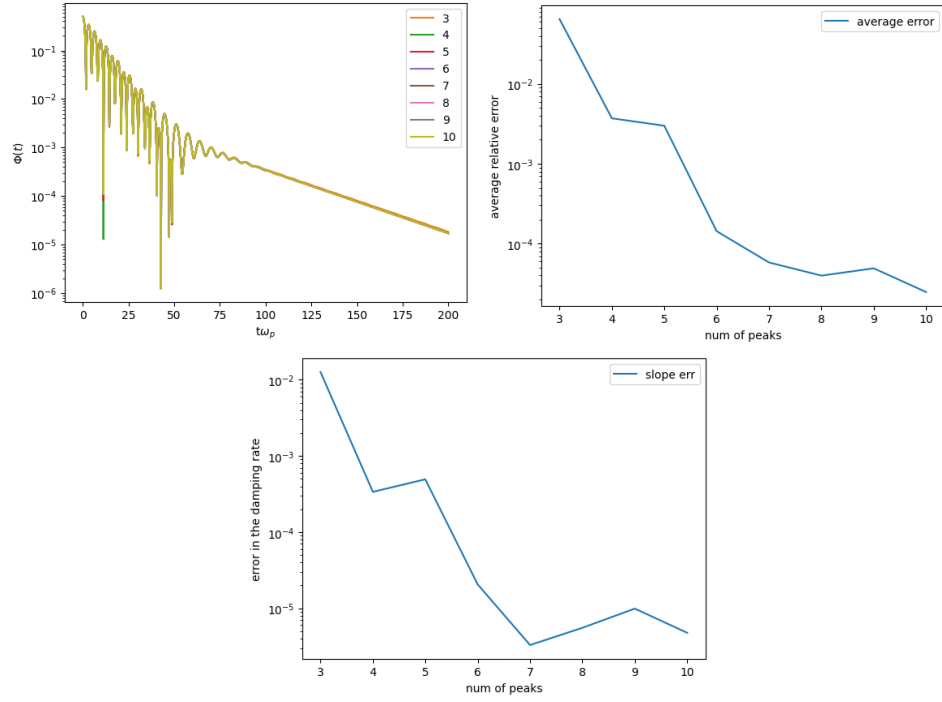
Figure 15: In the up-left figure, we can observe the different evolution of the electrostatic potential as a function of the m_1 parameter of the global filter. In the up-right figure, we see the average relative error between the approximated simulations and the real one. In the bottom figure, we can observe the relative error in the evaluation of the damping rate of the entropy mode.
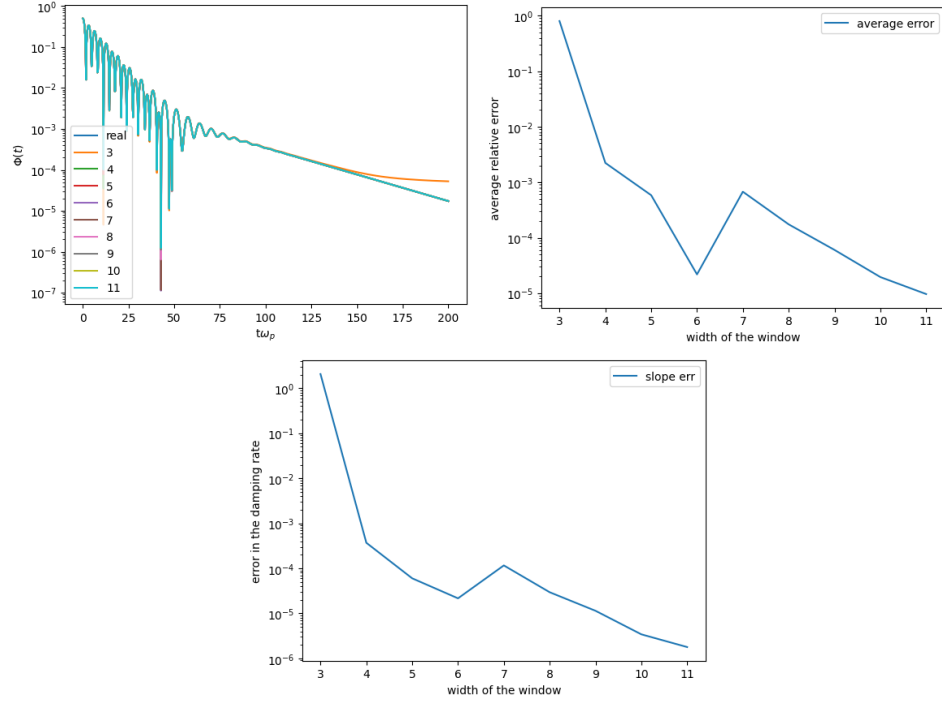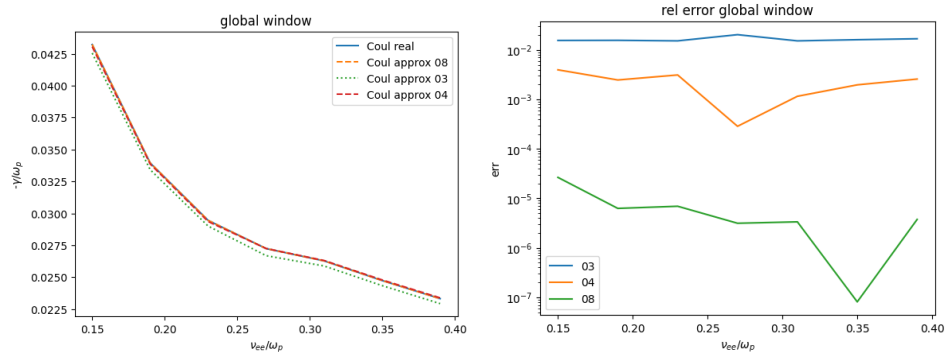
Figure 16: In the up-left figure, we can observe the different evolution of the electrostatic potential as a function of the m_2 parameter of the peak filter. In the up-right figure, we see the average relative error between the approximated simulations and the real one. In the bottom figure, we can observe the relative error in the evaluation of the damping rate of the entropy mode.

Figure 17: On the left, we can observe the different damping rates for the entropy mode computed at different collision frequencies ν/ω_p and through different approximations of the global filter.
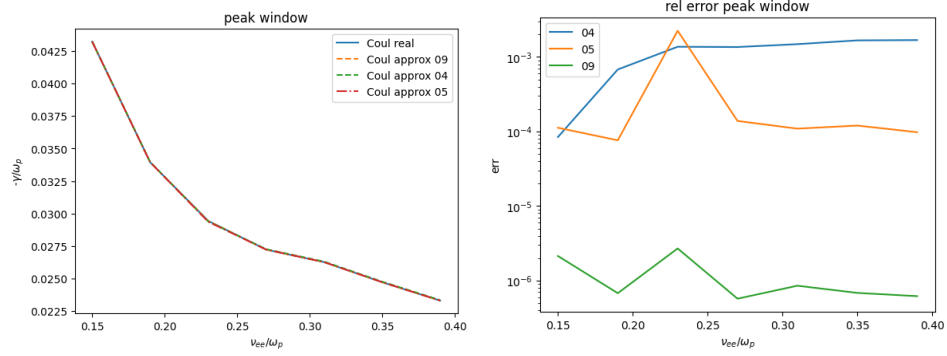
Figure 18: On the left, we can observe the different damping rates for the entropy mode computed at different collision frequencies ν/ω_p and through different approximations of the peak filter.
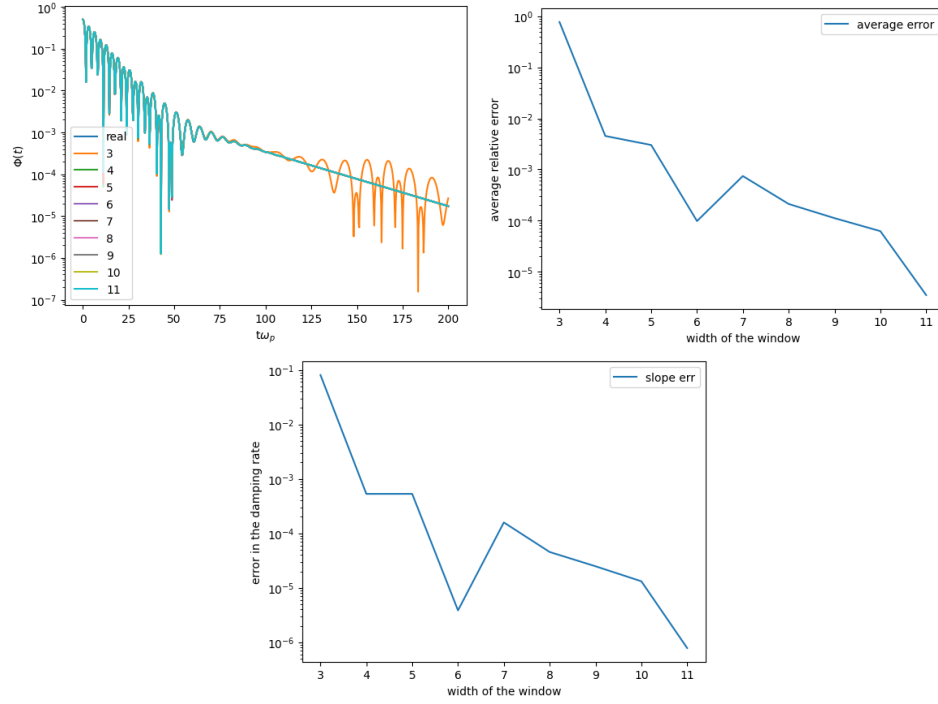

Figure 19: In the up-left figure, we can observe the different evolution of the electrostatic potential as a function of the parameters m_1, m_2, where we use $m_1 = m_2$. In the up-right figure, we see the average relative error between the approximated simulations and the real one. In the bottom figure, we can observe the relative error in the evaluation of the damping rate of the entropy mode.
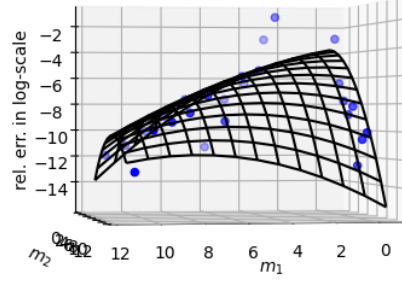
Figure 20: Least Squares fit in the m_1, m_2 plane of the error of the filters. On the z axis we have the relative error for the damping rate in log-scale.
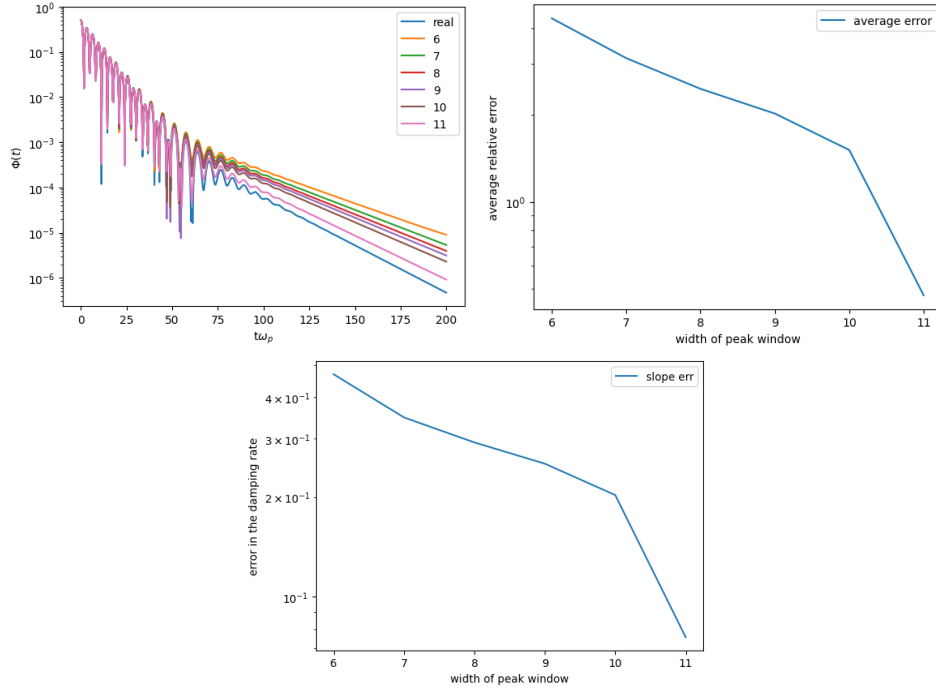

Figure 21: In up-left figure, we can observe the different evolution of the electrostatic potential as a function of the parameters m_2 of the peak filter applied to the electron-ion collision operator. In the up-right figure, we see the average relative error between the approximated simulations and the real one. In the bottom figure , we can observe the relative error in the evaluation of the damping rate of the entropy mode.

4   Conclusion

Overall, we can say that we managed to find meaningful patterns in the matrices of the collision operators, and we were also able to find good and meaningful approximations to extract the main information from the matrices. In the end, the approximations work really well for the electron-electron interaction term and poorly for the electron-ion interaction term. Future meaningful analyses would be testing the same filters with bigger matrices for the electron-ion interaction term and trying to generalize these filters to the case of the Gyrokinetic linear Coulomb collision operator since it presents a similar structure.

References

[1] B. FREI, J. BALL, A. HOFFMANN, R. JORGE, P. RICCI, and L. StENGER, "Development of advanced linearized gyrokinetic collision operators using a moment approach," *J. Plasma Phys*, 2021.

[2] R. HAZELTINE and J. MEISS, "Plasma confinement," *Courier Corporation*, 2003.

[3] W. MANDELL, N.R.and DORLAND and M. LANDREMAN, "Laguerre–hermite pseudo-spectral velocity formulation of gyrokinetics," *J. Plasma Phys*, 2018.

[4] B. FREI, R. JORGE, and P. RICCI, "A gyrokinetic model for the plasma periphery of tokamak devices," *J. Plasma Phys*, 2020.

[5] M. WONG, "The weyl transform," 1998.

[6] I. R. GRADSHTEYN, "Table of integrals, series, and products," 2014.

[7] X. XU and M. ROSENBLUTH, "Numerical simulation of ion-temperature-gradient-driven modes," *Phys. Fluids*, 1991.

[8] R. JORGE, B. FREI, and P. RICCI, "Nonlinear gyrokinetic coulomb collision operator." *J. Plasma Phys.*, 2019.

[9] W. ROSENBLUTH, M.N.and MACDONALD and D. JUDD, "Fokker–planck equation for an inverse-square force," *Physical Review 107 (1), 1.*, 1957.

[10] P. HELANDER and D. SIGMAR, "Collisional transport in magnetized plasmas," . *Cambridge University Press*, 2002.

[11] J.-Y. JI and E. HELD, "Exact linearized coulomb collision operator in the moment expansion," *Phys. Plasmas 13 (10)*, 2006.

[12] R. SNIDER, "Irreducible cartesian tensors," *De Gruyter Studies in Mathematical Physics, vol. 1. De Gruyter*, 2017.

[13] J. CARY, "1 lie transform perturbation theory for hamiltonian systems," *Phys. Rep. 79 (2), 129*, 1981.

[14] A. BERS, *Plasma Physics and Fusion Plasma Electrodynamics.* OUP Oxford, 2018.